January 2024

Misalignment effects on the physics performance of the inner tracker upgrade at the ALICE experiment

Jesper Gumprecht

Project duration: 9 months, 60 ECTS

Thesis submitted for Master of Science degree
Supervised by David Silvermyr

LUND
UNIVERSITY

Department of Physics
Division of Particle & Nuclear Physics

Abstract

This thesis deals with the physics performance of an approved inner tracker upgrade of the ALICE experiment involving a novel and ultra-thin silicon detector with a cylindrical geometry. During the thesis work, a method was developed in simulations to induce distortions to the detector's geometry, and the resulting loss in physics performance was evaluated. A strategy was also developed to be able to estimate the strength of the misalignment. Realignment could be performed using the estimated distortion strength to regain as much of the physics performance lost due to the distortions as possible.

Populärvetenskaplig beskrivning

Ett av de viktigaste målen inom experimentell fysik, om inte det viktigaste, är att utföra precisa mätningar för att nå bästa möjliga resultat. Inom högenergifysik görs mätningarna med hjälp av specialbyggda detektorer som bland annat finns vid världens största partikelaccelerator *the Large Hadron Collider* (LHC).

Vid LHC utförs flera experiment och ett av dessa är *A Large Ion Collider Experiment* (ALICE). ALICE-experimentets fokus är att studera kollisioner mellan tyngre joner. Experimentet består av ett flertal olika detektorer varav en kallas för *Inner Tracking System* (ITS). Det är ITS-detektorn som detta projekt fokuserar på.

Under regelbundna perioder stängs LHC ner vilket ger tillfälle för underhåll av experimenten och installation av eventuella uppgraderingar till olika detektorer. Under nästa längre nedstängningsperiod ska en banbrytande uppgradering av ITS-detektorn installeras och det är denna uppgradering som kommer utredas här.

ITS-detektorns primära ansvar är att rekonstruera spår från partiklar som producerats av kollisioner i ALICE-experimentet. För att bedöma detektorns prestanda är det vanligt att analysera olika variabler. Ett exempel på en sådan variabel är det minsta avståndet från spåret av varje rekonstruerade partikel till kollisionspunkten.

Under projektet har simuleringar använts för att utsätta den känsliga ITS-detektorn för mekaniska deformationer och därefter har prestandan utvärderats. Detta har använts för att utveckla en strategi som korrigerar för den mekaniska deformationen vilket lett till att prestandan återställts.

Acknowledgments

First of all, I would like to thank my supervisor, David Silvermyr, not only for giving me the opportunity to work on such an incredible project but also for all the help and guidance provided during this last year.

Secondly, I would also like to thank Fabrizio Grosa from CERN. I am grateful for all you have invested into this project, helping me with O^2, always answering my questions, and allowing me to present my work at the work package meetings.

Lastly, I would like to thank the entire September 2023 testbeam group. I especially want to thank Iaroslav and Stella, who made the testbeam experience one of the highlights of this project for me.

List of acronyms

ALICE A Large Ion Collider Experiment
ALPIDE ALICE PIxel DEtector
ATLAS A Toroidal LHC ApparatuS
CCDB Computer Center DataBase
CERN The European Organization for Nuclear Research
CMS Compact Muon Solenoid
DCA Distance of Closest Approach
GEM Gas-Electron Multipliers
ITS Inner Tracker System
LHC Large Hadron Collider
LHCb Large Hadron Collider beauty
MOSS MOnolithic Stitched Sensor
MWPC Multi-Wire Proportional Chambers
O^2 OnlineOffline
PS Proton Synchrotron
QGP Quark Gluon Plasma
RHIC Relativistic Heavy Ion Collider
RICH Ring-imaging Cherenkov
ROF Read-Out Frame
SDD Silicon Drift Detector
SPD Silicon Pixel Detector
SPS Super Proton Synchrotron
SSD Silicon Strip Detector

Contents

Chapter 1

Introduction

One of the most successful theories in physics is the Standard Model[1], which describes the elementary particles and how they interact via three of the four fundamental forces. The reason behind the model's success stems from all the theoretical predictions one has been able to make, together with the precision of the experimental verification. Maybe the most famous example is the discovery of the Higgs boson. Initially, the theory of the boson was suggested in a paper published in 1964 by Peter Higgs [2], and it was not until 2012, almost 50 years later, that Higgs' theory was eventually verified [3, 4].

For scientific breakthroughs at the high-energy frontier of particle physics, like the Higgs discovery, to take place, large-scale experiments are required. Several such experiments can be found at the largest particle accelerator in the world, the LHC (Large Hadron Collider), located at CERN close to Geneva, on the border between France and Switzerland. The experiment relevant to this thesis is ALICE (A Large Ion Collider Experiment) [5]. The ALICE experiment focuses on high-energy heavy-ion physics by studying collisions of lead nuclei (Pb−Pb). It is a large detector being 26 m long, 16 m high, and 16 m wide, with various components to gather as much information as possible about the particles produced in these collisions [6].

The component closest to the beamline at the ALICE experiment is the ITS (Inner Tracking System), and this part of the experiment is responsible for reconstructing tracks and vertices for charged particles. The ITS itself consists of silicon detectors in several layers located at increasing radii away from the beamline. The original ITS had six layers, but during Long Shutdown 2 (2019-2021), an upgrade to the tracking system was installed with a new design to improve reconstruction efficiency. The ITS2 upgrade was also installed with an additional cylindrical layer, i.e., with a total of seven layers.

[1]For a review of the Standard Model, see, e.g., "*An Introduction to the Standard Model of Particle Physics*", by W. N. Cottingham and D. A. Greenwood [1].

A new upgrade following the ITS2 has been proposed, the ITS3, which is to be installed during Long Shutdown 3 (2026-2028)[2]. Unlike the ITS2 upgrade, which replaced the entire inner tracking system, the ITS3 will only replace the three innermost layers and further improve tracking efficiency. The project discussed in this thesis investigates the effects on vertex and track reconstruction that a geometrical distortion can induce. The vertex and track reconstruction algorithms have been adjusted to the ITS3 in a new framework, O^2 (OnlineOffline) [7], developed by the ALICE collaboration for analysis and simulations.

The ITS3 upgrade seeks to implement novel scintillator technology that seeks to reduce the material budget of the inner layers to only 0.05% X_0 in each layer, which has never been done before. This new detector would be thin enough to be bent about the axis of the beam, making it mechanically self-supportive, removing the need for supporting material.

The thin and bent ITS3 is susceptible to mechanical deformation during production or installation, which is the topic of this thesis, and the potential effect mechanical deformations could have on physics performance will be presented. Furthermore, preliminary work on realignment to recover as much performance as possible is also discussed within the thesis.

[2]The schedule as of writing this thesis. Subject to change.

Chapter 2

Theoretical and experimental background

An introduction to software, simulations, and variables for evaluating physics performance is instead discussed in Chap. 3.

2.1 The Standard Model

The Standard Model [1] is the primary theory in particle physics describing the fundamental particles and force carriers, which are shown in Fig 2.1. This model describes weak, strong, and electromagnetic interactions but does not incorporate gravity. Quantum numbers, such as spin, characterize particles. Particles either have integer or half-integer spin. Particles with integer spin are called *bosons*, and particles with half-integer spin are called *fermions*. The major difference between bosons and fermions, apart from their spin, is that fermions must abide *the Pauli Exclusion Principle*, which states that two particles in the same system cannot occupy the same quantum state. This indicates a difference in statistical behavior between fermions and bosons, and these behaviors are commonly referred to as *Bose-Einstein* statistics (bosons) and *Fermi-Dirac* statistics (fermions) [8].

There are three *up-like* quarks (u, c, t) and three *down-like* quarks (d, s, b), usually divided into three generations. Up-like quarks carry a charge of $+2/3$, and down-like quarks, a charge of $-1/3$, expressed in terms of the elementary charge, e. There are two types of leptons. Charged leptons that carry a charge of -1, and neutral leptons (neutrinos) that have no charge. The anti-particles of quarks and leptons carry the opposite quantum numbers, such as charge, but they have the same mass.

The major difference between quarks and leptons is that quarks carry a color charge (referred to as red, green, or blue) and have to adhere to what is described by QCD (Quantum

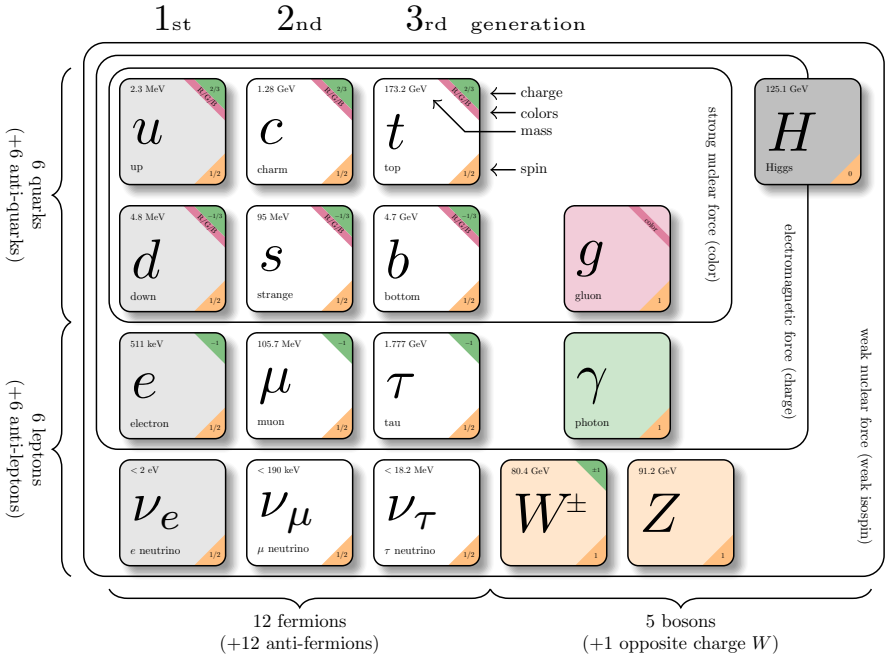

Figure 2.1: A schematic of the Standard Model modified from Ref. [9] that shows all the fundamental particles and force carriers.

Chromodynamics) as *color confinement*, while leptons are color-free. Confinement requires quarks to exist in color-neutral groups (commonly referred to as *hadrons*) bound by the strong force. Hadrons can be further categorized as either *mesons* or *baryons*. Mesons comprise two quarks, one quark with a color charge and one anti-quark with an anti-color charge. Baryons are made up of three quarks and achieve a neutral color by each quark having a different color charge. Since quantum numbers are additive, mesons will have an integer spin, and baryons will have a half-integer spin. Therefore, as illustrated in Fig. 2.2, mesons follow Bose-Einstein statistics and baryons follow Fermi-Dirac statistics.

The quarks having a color charge is what allows the quarks to interact with gluons, which are the carriers for the strong force. Gluons are massless bosons with a color and anti-color charge, and have no electrical charge. All fermions that carry electric charge can also interact electromagnetically through photons, which mediate the electromagnetic force. The force carriers for the weak force are the Z^0 and the $W^{\pm}$, which can interact with all fermions.

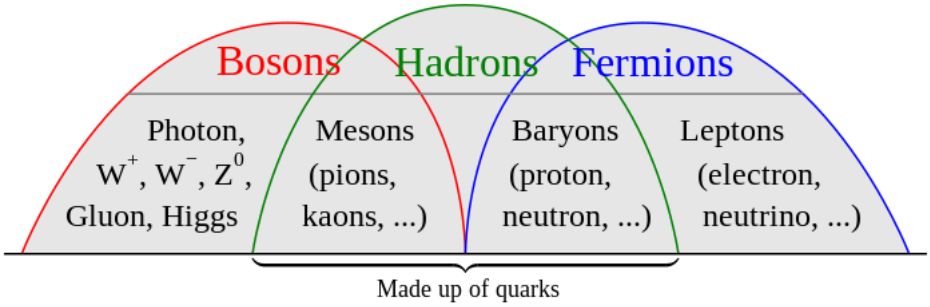

Figure 2.2: Illustration of how composite particles are categorized as bosons and fermions. Figure from Ref. [10].

2.2 Quark Gluon Plasma

As explained earlier, quarks and gluons are confined in hadrons. However, it has been suggested that a state of matter exists where the quarks and gluons are no longer confined, but instead exist in a 'quark soup' called QGP (Quark-Gluon Plasma) [11]. It is believed that just after the Big Bang, the matter existed in such a state for a few microseconds before undergoing *hadronization*. Hadronization is the process of quarks and gluons of the QGP form into hadrons.

It is suggested that conditions in high-energy nucleus-nucleus collisions at the accelerator LHC produce enough heat and pressure to allow the QGP phase to exist. Because these conditions are only present during the collision, it becomes impossible to maintain the state of a QGP long enough to study its characteristics directly. Therefore, to study QGP, one instead investigates the effects of the QGP, such as *strangeness enhancement* [12] or *collective flow* [13]. For the later sections of this thesis, dealing with detector development, it is important to note that in these nucleus-nucleus collisions at LHC, several thousands of particles will be produced in single collisions, and they need to be individually tracked and identified.

2.3 Multiple scattering and material budget

If a charged particle travels through a material, it will likely interact with the material using the Coulomb force [14]. As a result of one Coulomb interaction, the particle will slow down and scatter from the initial path. If the material is not very thin, the particle would probably continue to interact and scatter with additional nuclei and electrons while traversing the material. This phenomenon is known as multiple scattering, and it occurs whenever a charged particle travels through any material [15].

When it is of interest to reconstruct particle tracks after a collision, several layers of

detectors are needed to be able to reconstruct the particle's initial path correctly. However, due to multiple scattering, as a particle travels through the first layer, its trajectory will be affected. Consequently, the precision of reconstructing the initial path deteriorates, and one might not achieve the desired performance. As a result, to reduce the influence of multiple scattering, the less material used for the tracking detector, the better. One would, therefore, like to quantize the thickness of the material, and it is commonly done with respect to the radiation length, X_0 [16]. The radiation length is defined by the mean path length required for a relativistic electron's energy to be reduced by a factor of $1/e$. Material budget is usually expressed in terms of X_0, e.g., 0.5% X_0.

2.4 Mean energy loss for charged particles

Charged particles traversing a medium will lose energy over some traveled distance, x. The mean energy loss of charged particles ($\mathrm{d}E/\mathrm{d}x$) can then be estimated by the Bethe-Bloch formula [17],

$$-\frac{\mathrm{d}E}{\mathrm{d}x} = \frac{4\pi\alpha^2 h^2}{m_e}\frac{q^2 n_e}{\beta^2}\left[\ln\left(\frac{2m_e c^2\beta^2\gamma^2}{I}\right) - \beta^2 - \frac{\delta(\gamma)}{2}\right]. \tag{2.1}$$

The variables in this equation can be grouped into three categories: natural constants, particle-dependent, and material-dependent variables. The natural constants included in the equation is the fine structure constant, α, the electron mass, m_e, and Planck's constant, h. Variables dependent on the particle are the charge, q, and the Lorentz factor, γ, and β, which is the velocity, v, divided by the speed of light, c. Variables dependent on the material traversed by the particle is the mean of the ionization potential, I, and the electron density, n_e. Lastly, $\delta(\gamma)$ is a correction term for relativistic particles that describe dielectric screening.

2.5 Definition of common variables

2.5.1 Coordinate system

The coordinate system at the ALICE experiment [18] is defined as follows:

- $x - axis$: orthogonal to the beam and aligned with the horizontal plane, pointing towards the center of the LHC;
- $y - axis$: orthogonal to the beam and aligned with the vertical plane, pointing upwards;
- $z - axis$: parallel to the beam direction, pointing towards the CERN Meyrin site (Point 1);

- *azimuthal angle* φ: from $x - axis$ to $y - axis$;
- *polar angle* θ: from $z - axis$ to $xy - plane$.

Therefore, the conversion between Cartesian and spherical coordinates is given by:

$$\begin{aligned} x &= r \sin\theta \cos\varphi, \\ y &= r \sin\theta \sin\varphi, \\ z &= r \cos\theta. \end{aligned} \tag{2.2}$$

2.5.2 Transverse momentum

Detectors usually have their coordinate system defined such that the beam axis coincides with the $z - axis$. In ALICE, the momentum of a particle is determined by its bend in azimuth φ in the $xy - plane$. Therefore, measuring the momentum's x and y components is relatively straightforward for detectors with a coaxial structure. This is also the momentum in the transverse plane, usually denoted as p_T, and defined as

$$p_T = \sqrt{p_x^2 + p_y^2}. \tag{2.3}$$

The particles in the colliding beams only have momentum in the z direction; therefore, their p_T is zero, which is one of the reasons the observable p_T is commonly used in data analysis.

2.5.3 Rapidity and psuedorapidity

The LHC accelerates particles to a velocity close to the speed of light, and for that reason, one has to treat the particles as relativistic in calculations. Consequently, the quantity *rapidity*, denoted as y, has been introduced. Rapidity has the property that it is additive between different Lorentz frames, and is defined as,

$$y = \ln \frac{E + p_z}{E - p_z} = \operatorname{arctanh} \beta_z, \tag{2.4}$$

where p_z and β_z is the particle's momentum and velocity relative to the speed of light in the beam direction, and E is the energy of the particle defined as

$$E = \sqrt{m^2 + \boldsymbol{p}^2}, \tag{2.5}$$

where m is the mass of the particle, and $\boldsymbol{p}$ is the total momentum. This means that to determine the rapidity, one needs the mass, total momentum, and velocity of a particle, which can be rather cumbersome to achieve for each of the thousands of relativistic particles

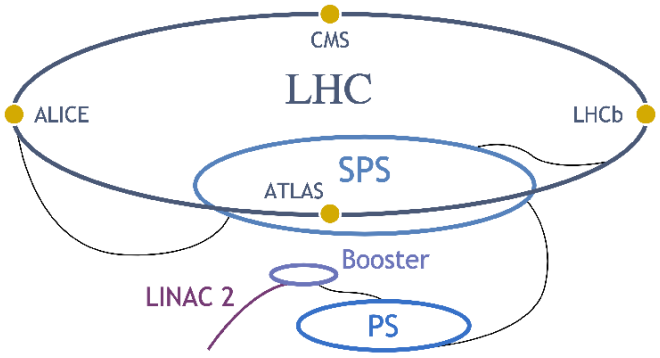

Figure 2.3: Schematic overview of the LHC and the four largest experiments. It also shows the SPS and the PS that are used as injectors for the LHC. Figure from Ref. [23]

produced in a single collision. However, for relativistic particles, one can approximate the total energy as

$$E \approx |\boldsymbol{p}|, \quad \text{for} \quad m \ll |\boldsymbol{p}|. \tag{2.6}$$

This allows us to approximate the rapidity, and this approximated quantity is known as *pseudorapidity* and is denoted by η. The pseudorapidity is defined as

$$\eta = \frac{1}{2} \ln \frac{|\boldsymbol{p}| + p_z}{|\boldsymbol{p}| - p_z} = -\ln \tan \frac{\theta}{2}, \tag{2.7}$$

which means that it only depends on the polar angle, θ.

2.6 The Large Hadron Collider

In 2008, on the 10th of September, the LHC was started for the first time [19] and became the highest energy particle accelerator in the world. The 27 km long accelerator is operated by CERN (The European Organization for Nuclear Research) at the France-Switzerland border. It accelerates heavy nuclei or protons to speeds slightly below the speed of light. In total, CERN operates nine different accelerators. Accelerators like the SPS (Super Proton Synchrotron) are not only used for experiments but also to prepare particles to be injected into the LHC. Likewise, the PS (Proton Synchrotron) is used for experiments and to prepare particles to be injected into the SPS. In Fig. 2.3, the overview of LHC is shown with its four major experiments. The two larger experiments are ATLAS (A Toroidal LHC ApparatuS) [20] and CMS (Compact Muon Solenoid) [21]. The other two experiments are ALICE and LHCb (Large Hadron Collider beauty) [22].

ATLAS and CMS are two *general-purpose* experiments, investigating topics such as the Higgs boson, and physics beyond the Standard Model, such as dark matter, or even searching for extra dimensions [24, 25]. LHCb is an experiment dedicated to studies of the *bottom*

(also known as *beauty*) quark and explores physics regarding matter and antimatter [26]. The ALICE experiment explores heavy-ion physics and investigates the state of matter that is QGP [6]. During a year at the LHC, there is proton physics for about seven months and heavy-ion physics for one month. Despite only having Pb-Pb collisions for one month, the ALICE experiment still takes p-p data and some cosmic data during the rest of the data-taking period.

Chapter 3

A Large Ion Collider Experiment

The ALICE experiment is located in Saint-Genis-Pouilly in France, or Point 2 at the LHC, and focuses on heavy-ion physics, where one of the main goals is to describe QGP and understand the properties of deconfinement in QCD. The experiment has several different detectors installed, shown in Fig. 3.1. Different detector subsystems have different areas of focus, such as particle tracking or particle identification.

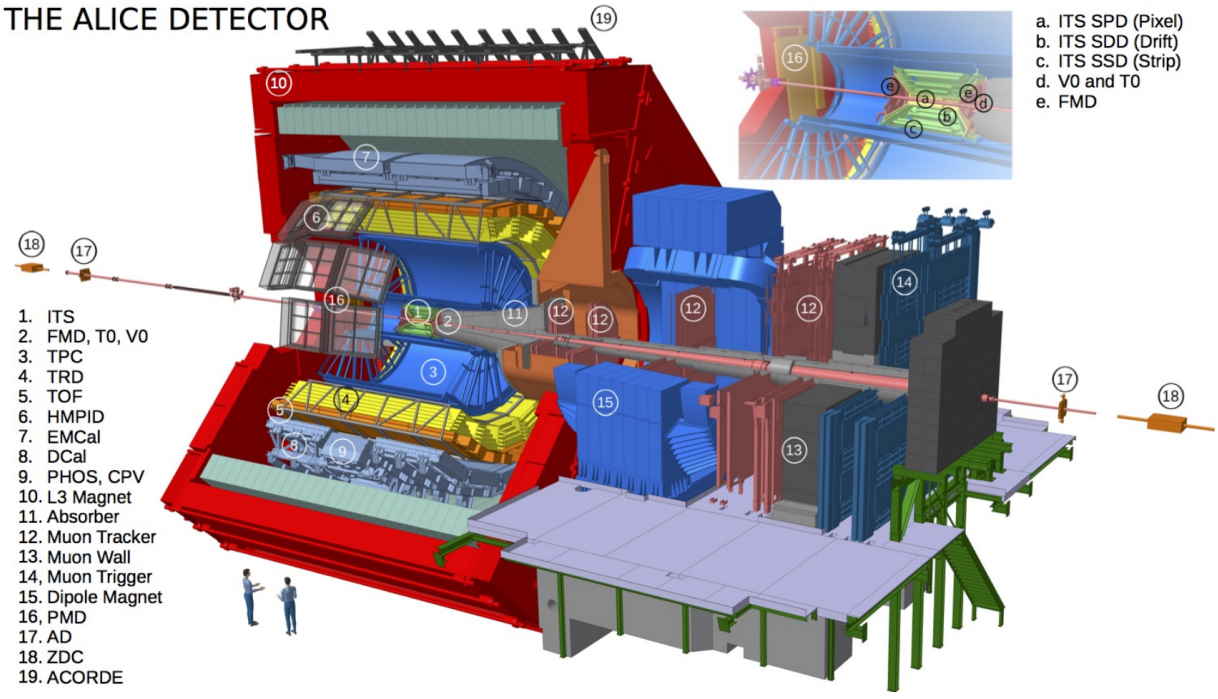

Figure 3.1: Illustration of the structure of the ALICE experiment, showing where each detector subsystem is located. Picture from Ref. [27]. It was published in 2017, meaning that upgrades installed during LHC Long Shutdown 2 are not included in this schematic.

The main detectors for tracking charged particles are the ITS (Inner Tracking System) and TPC (Time-Projection-Chamber) [28], and these will later be described more thoroughly. Together with the ITS and the TPC, in the central barrel of the experiment, the TOF (Time-Of-Flight) detector is responsible for identifying charged particles with momentum values up to a few of GeV/c [29]. Covering parts of the acceptance of the central barrel are subsystems such as the EMCal (Electro-Magnetic Calorimeter), PHOS (PHOton Spectrometer), and the HMPID (High Momentum Particle Identification Detector). The EMCal and PHOS are both electromagnetic calorimeters, and the HMPID is a RICH (Ring-Imaging Cherenkov) detector that focuses on identifying particles with higher momentum.

3.1 Inner Tracking System

The ITS was first installed with the purpose of improving primary and secondary vertex reconstruction, track particles with momentum too low to be detected in the TPC, and also to improve the momentum resolution for particles reconstructed by the TPC [30]. It consisted of six layers with three different types of detectors,

- Two inner layers: SPD (Silicon Pixel Detector),
- Two middle layers: SDD (Silicon Drift Detector),
- Two outer layers: SSD (Silicon Strip Detector),

where each layer had a material budget of approximately 1% X_0 [5]. For more information about these detectors, see Ref. [31], the Technical Design Report for the ITS, which contains detailed explinations.

3.1.1 ITS2: Long Shutdown 2 upgrade

An upgrade of the ITS (ITS2) was installed during LHC Long Shutdown 2 (2019-2021), where the entire detector was replaced, and the addition of a seventh layer. Each layer is equipped with ALPIDE (ALICE PIxel DEtector) chips, a Monolithic Active Pixel Sensor [32]. The ALPIDEs are mounted on staves, which are angled such that they overlap, to ensure full azimuthal coverage. This upgrade aimed to reduce both the material budget and to have measurements closer to the collision point to improve the resolution of the track impact parameter [33]. This made it possible to improve the efficiency of track reconstruction and the resolution of the reconstructed p_T. The ITS2 detector is divided into the Inner and Outer Barrel, where the Inner Barrel is the three innermost layers, and the Outer Barrel is the four outermost layers. The Outer Barrel is also sometimes described as the Middle and Outer Layers. In the Inner Barrel, one reduced the material

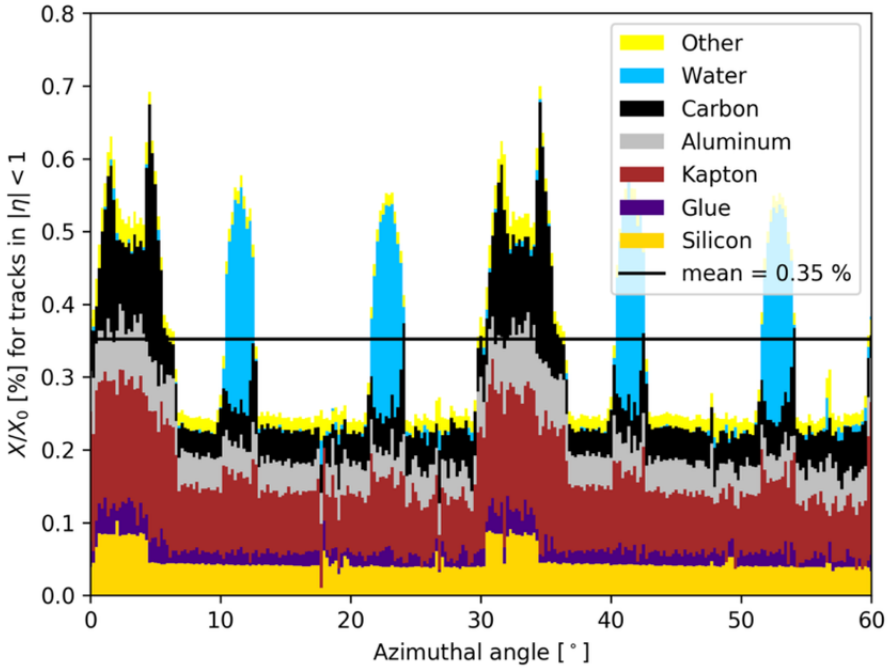

Figure 3.2: Material budget for a layer in the Inner Barrel. Figure from Ref. [34].

budget to approximately 0.35% X_0 per inner layer, and in the Outer Barrel, down to 0.8% X_0 per outer layer.

In Fig. 3.2, the material budget for one of the Inner Layers is shown, and in this figure, one can see that the silicon detector itself only makes up a fraction of the material budget. We can see that the larger contributions to the material budget are materials used for cooling and mechanical support. The mechanical structure of the ITS2 is complex (shown in Fig. 3.3), and it is not trivial to further reduce the contributions to the material budget from mechanical support. This observation is the premise and motivation for another upgrade of the ITS (ITS3).

3.1.2 ITS3: Approved upgrade for Long Shutdown 3

The proposed and approved ITS3 upgrade will fully replace the staves in the Inner Barrel of the ITS2 with a very thin sensor that one can bend [35]. Such a structure would mechanically be mostly self-supporting, allowing for a large reduction in material budget. A schematic of the ITS3 is shown in Fig. 3.4, where one can see the cylindrical structure of the silicon layers.

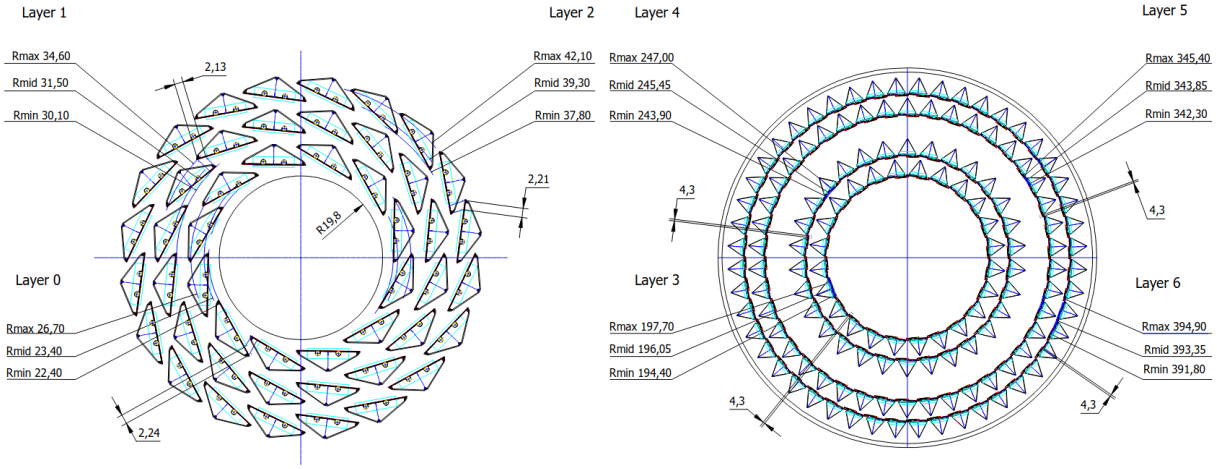

Figure 3.3: The $xy-plane$ of the ITS2 with the Inner Barrel in the left part of the figure and the Outer Barrel in the right part. Figure from Ref. [28]. Measurements are given in millimeters.

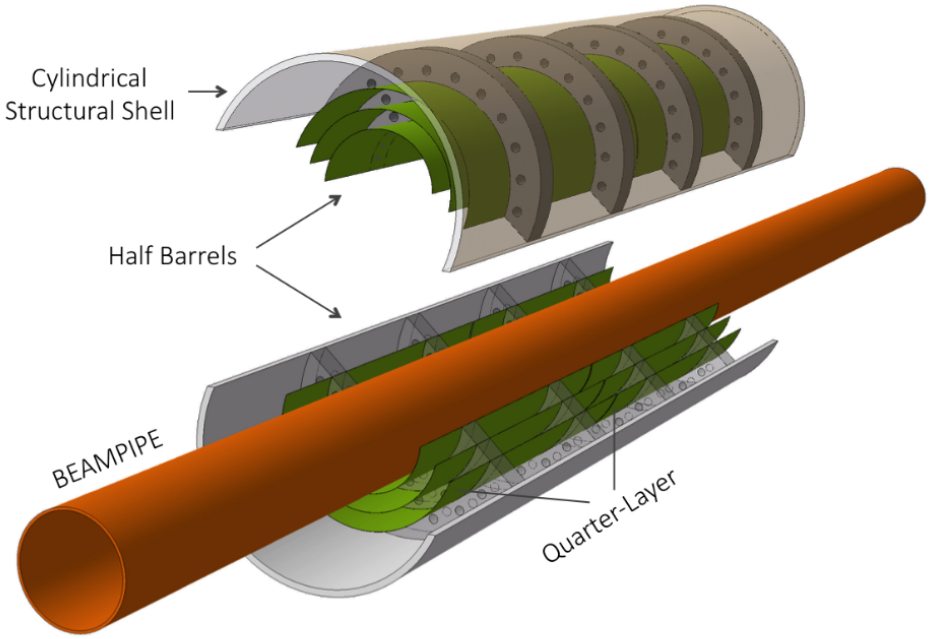

Figure 3.4: Structural layout of the ITS3. Each layer consists of two separate silicon detectors that have been bent into a half-cylindrical shape. Figure from Ref. [35].

Figure 3.5: Pitcure by the author of a MOSS prototype connected to a printed circuit board, used for testing at the PS in September 2023. The MOSS is made up of ten units, divided into half-units, and each half-unit is made up of four matrices.

As a consequence of the removal of much of the previously required mechanical supportive structure, air may more freely flow through the detector, and it is thought that cooling through the airflow is enough for the detector, which would allow for even further reduction in the material budget. By removing the contributions from cooling and mechanical support, the material budget in the Inner Barrel would be reduced to an unprecedented 0.05% X_0 in each layer. Furthermore, the ITS3, with its first layer even closer to the beampipe than the ITS2, is also expected to increase efficiency at low p_T and significantly improve the precision of track reconstruction.

Prototype chips for the ITS3 have been developed for testing, and one such prototype is called a MOSS (MOnolithic Stitched Sensor) [36]. The MOSS shown in Fig. 3.5 is attached to a printed circuit board with five sockets for proximity boards used for data acquisition in testing. Each of the five sockets connects to different units on the MOSS. Each unit has one top half and one bottom half, which have slightly different characteristics. The top half-units have 256x256 pixels with a pixel pitch[1] of 22.5 µm, and the bottom half-units have 320x320 pixels with a pixel pitch of 18 µm. One of the goals with the MOSS tests is to settle on the pixel pitch value for the final ITS3 detector. The MOSS is 25.9 cm wide and has a height of 1.4 cm. The MOSS shown in Fig. 3.5 was not bent for testing. However, when other prototypes, similar to the one in the figure, are bent, they would be bent into a cylindrical shape about the horizontal axis.

[1]Pixel pitch is the distance between pixels.

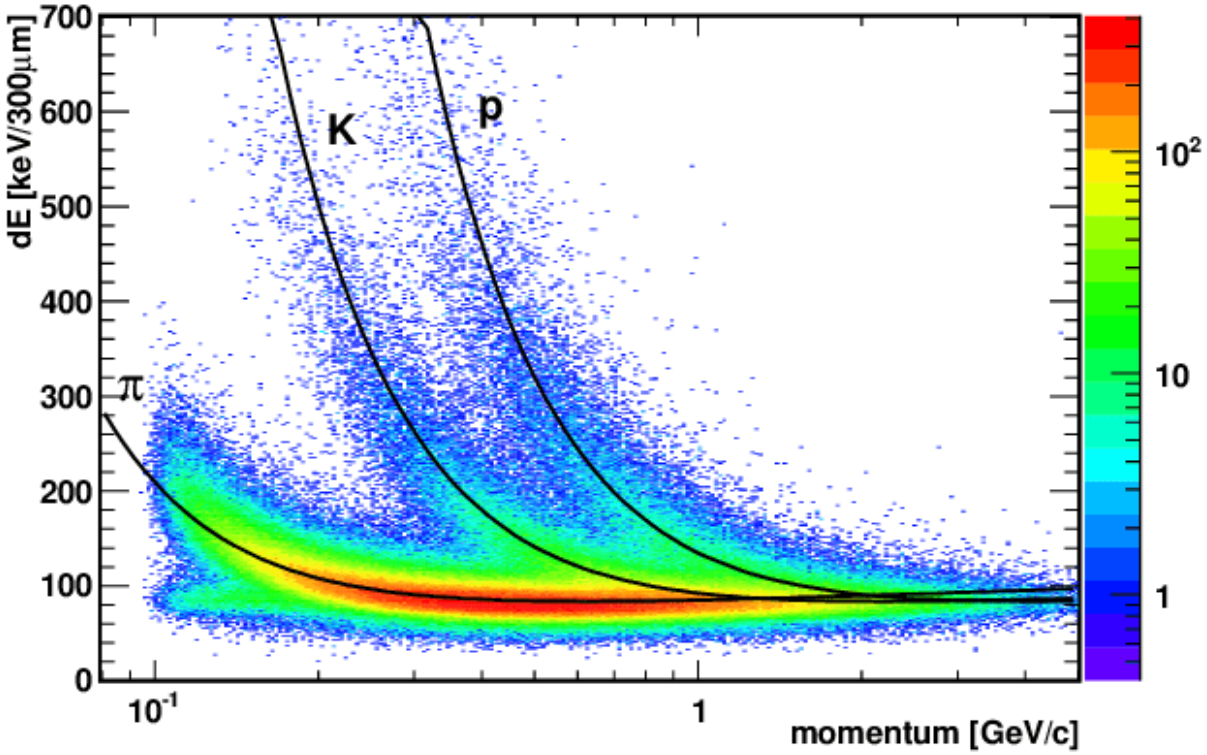

Figure 3.6: Example of measured energy loss at the ITS used for particle identification. Included in the histogram is the expected energy loss computed using the Bethe-Bloch formula. Figure from Ref. [37].

3.1.3 Particle identification with the ITS

The ITS is not only used for track reconstruction but also for particle identification. Extracting the p_T from the curvature of the requested track and measuring the energy deposit for a particle at each layer allows one to identify low-momentum particles [38]. This is illustrated in Fig. 3.6, and in this figure, one can see that pions, kaons, and protons can be reasonably well separated for $p_T < 1$ GeV/c.

3.2 Time-Projection Chamber

The TPC is often considered the main device for tracking and identifying charged particles in ALICE. It is a large gas-filled cylinder surrounding the ITS, which can be seen in Fig. 3.1. Several major components of the TPC are shown in Fig. 3.7. The inner and outer field cage define the drift volume, and the endplates keep the field cage together. Furthermore, it is through the endplates that readout equipment is connected. During

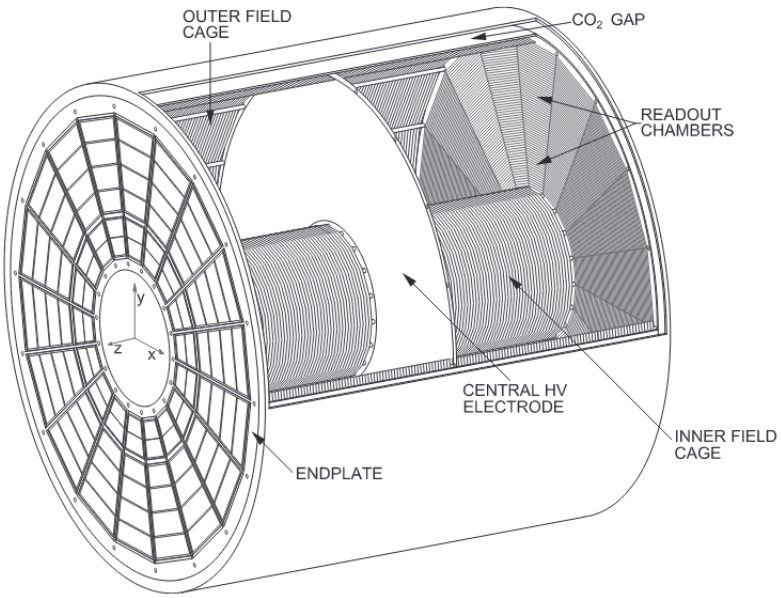

Figure 3.7: Schematic of the major components of the TPC. Figure from Ref. [39].

LHC Long Shutdown 2, the readout chambers were upgraded from MWPCs (Multi-Wire Proportional Chambers) to GEMs (Gas-Electron Multipliers).

3.2.1 Using the TPC for reconstruction

Filling the hollow space within the cylinder is a composite gas, Ne-CO_2-N_2 (90-10-5) [39]. When charged particles traverse this gas, the gas is ionized. A uniform electric field is applied from the central HV to the endplates, which causes the freed electrons to drift towards the endplates. Signals are detected once the electrons reach the endplates, and spatial coordinates in x & y can be reconstructed. In order to reconstruct the z coordinate, the time it takes from the gas to be ionized to a signal seen in the readout chambers is measured. This time is called the drift time. Shown in Fig. 3.1 as item 10, the L3 magnet provides a magnetic field along the $z - axis$ at the experiment. When a charged particle traverses a magnetic field parallel to its direction, it will curve. This makes it possible to compute the transverse momenta [41],

$$\rho = \frac{mv_\perp}{qB} = \frac{p_T}{qB} \rightarrow p_T = qB\rho, \tag{3.1}$$

where m and q are the mass and charge of the particle, $v_\perp$ is the particle's velocity perpendicular to the magnetic field, B is the magnetic field, and ρ is the curvature. The ionization energy loss ($\mathrm{d}E/\mathrm{d}x$) is measured up to 159 times for a charged particle in the TPC [41].

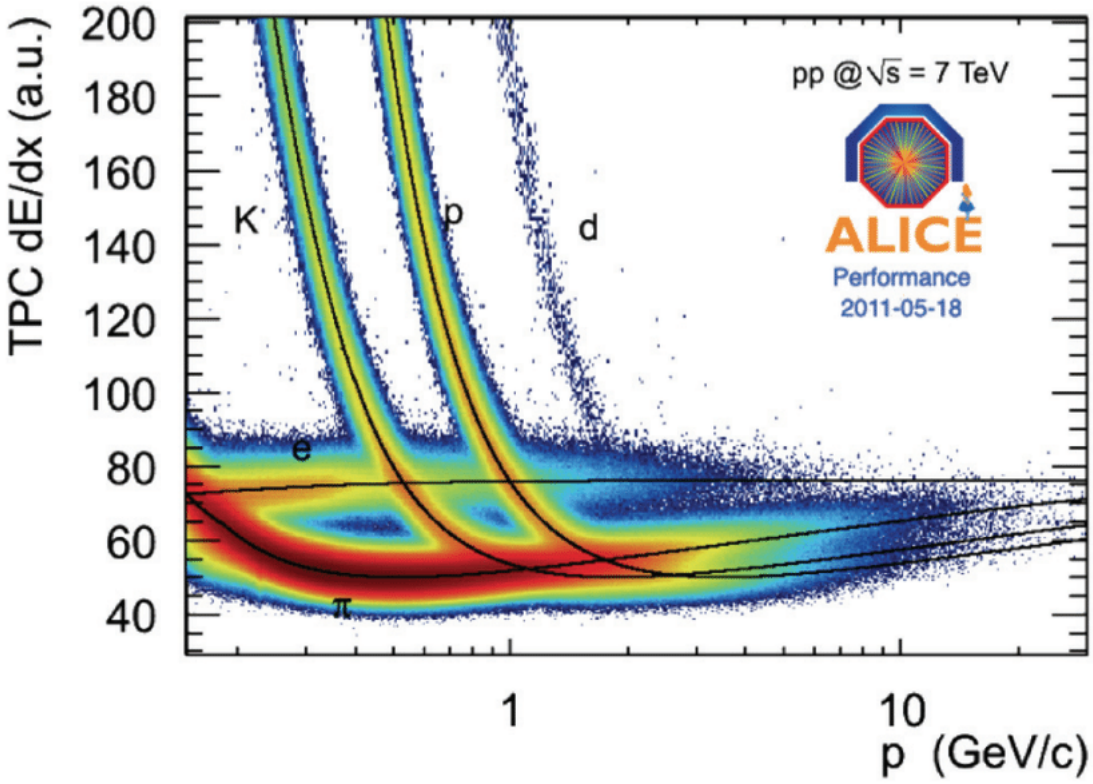

Figure 3.8: Example of measured energy loss at the TPC used for particle identification. Shown in the histogram as black lines are also the expected energy loss for each particle. Figure from Ref. [40].

3.2.2 Particle identification with the TPC

Similar to the ITS, the TPC also uses the mean energy loss and the transverse momentum for particle identification, shown in Fig. 3.8. As can be seen in the figure, pions and kaons can be separated up to a p_T of approximately 0.6 GeV/c. Kaons and protons are also separable up to approximately 1.1 GeV/c, and at higher momentum, one can do statistical particle identification analyses, even if it can be challenging to identify each individual particle separately.

Chapter 4

Software and simulations

This project strictly involves ITS standalone simulations. This means that reconstruction was only done with information provided directly by the ITS. Simulations were done using the O^2 [7] computing framework developed by the ALICE collaboration. Analysis was done using the `ROOT` framework [42]. Both of these frameworks were developed in `C++`.

4.1 O^2 and O^2Physics

O^2 and O^2Physics are tools for LHC Run 3 and 4 data simulation and analysis in ALICE [43]. A simulation in O^2 is processed in multiple steps, beginning with the event generation and transport. Then, digitization is performed, which converts the energy deposits, *hits*, from the transportation to detector signals, *digits*, to mimic the detector output. The last step is the reconstruction, in which the digits are clustered, and vertexing and tracking are performed. Then, for data analysis of either a simulation from O^2 or Run 3 data, one uses O^2Physics.

4.1.1 Event generation and particle transport

The event generator `PYTHIA8` [44] is integrated with O^2 and used by default. It is the generator used in this project, with mostly default settings, to simulate p−p collisions. The only parameter altered is the `PhaseSpace` parameter, which allows one to set constraints on the kinematics. This was done to get more statistics for higher p_T; the used values were:

```
PhaseSpace:pTHatMin = 30.
PhaseSpace:pTHatMax = 1000.
```

The corresponding default values are:

PhaseSpace:pTHatMin = 0.
PhaseSpace:pTHatMax = −1.

where a value of `pTHatMax` smaller than `pTHatMax` results in there being no upper limit [45].

O^2 has several available integrated options for particle transport. In this work, `Geant4` [46] with default parameters was used. Once events have been generated and transported, files containing kinematics, detector response, and Monte Carlo information are created.

4.1.2 Digitization and clustering

When a charged particle encounters an ITS detector, an electronic signal is sent from the pixel on one of the detector chips that was hit by the particle. Silicon pixel detectors can be characterized by the number of pixels and pixel pitch, which indicates that the detector's coverage is not continuous but instead restricted by these characteristics. This is not the case for the hits generated by the Monte Carlo simulation, as the hits are continuously spread amongst the defined detector geometry. Therefore, digitization has to be performed, translating the continuous hits into discrete digits in the corresponding pixel positions of the detector. Once this is done, the data format in the simulation is the same as for real detector output. Consequently, this allows one to perform the same reconstruction on simulations and real data.

In practice, a charged particle passing through a detector could fire more than one pixel. In other words, multiple digits might belong to the same particle. For that reason, the first step of reconstruction is to group digits that are thought to belong to the same particle in clusters. This is a rather small effect. In the MOSS test in September, the average varied from 1.01 to 1.07 pixels per cluster in the testbeam data, depending on which unit (top or bottom) and which region[1] was under study.

4.1.3 Primary vertex reconstruction

A primary vertex is where two nuclei, or protons, from the incoming beams, initially collide at the interaction point, given in three-dimensional coordinates. The first goal of the reconstruction is to find the primary vertex using only the data recorded by the detector. This section discusses the outline of the preliminary procedure for reconstructing primary vertices using only information from the ITS, presented in Ref. [47]. More complex algorithms are used later in the reconstruction workflow, using information from other detectors to improve the accuracy further.

Two separate clusters from different layers can be connected using straight lines, and these

[1] As mentioned earlier, each half-unit has four matrices. These are also referred to as regions.

lines are known as track *candidates*. A candidate is not a reconstructed track but rather a starting point for both primary vertex and track reconstruction. These track candidates are also referred to as *tracklets*.

The first step is to identify tracklets and perform a selection regarding which to use for the reconstruction. The selected tracklets have clusters on consecutive layers. Since the Inner Barrel has three layers, selected tracklets will have clusters on either layers 0 and 1 (inner tracklets) or layers 1 and 2 (outer tracklets). The layer numbering for the ITS3 follows the same pattern as the ITS2, where layer 0 is the innermost layer and increases outwards (labels are shown in Fig. 3.3). The inner and outer tracklets are then matched into one merged tracklet intersecting all three layers. Tracklet matching is done through an iterative approach. One iterates over all outer tracklets for each inner tracklet, attempting to merge them. As soon as a set of conditions is met, the merged tracklet is accepted, and the iteration starts for the next inner tracklet. These conditions are:

- both the inner and outer tracklet must share a cluster on layer 1,
- the relative inclination between the inner and outer tracklets must not exceed a given threshold on either the $xy - plane$ or the $rz - plane$.

If no outer tracklet meets the conditions, the tracklet is discarded.

The last step is to find the primary vertex using the accepted merged tracklets. By nested iterations, the *centroids* can be computed for all different combinations of merged tracklets. The centroid of two merged tracklets is the point that is closest to both lines. Once all centroids have been computed, histograms can be filled for each Cartesian coordinate, and in this way, primary vertices can be estimated.

It is important to understand that all reconstructed vertices do not necessarily correspond to *real* vertices. In simulations, we can access the so-called Monte Carlo *truth*, which contains the *true* information about each generated particle and clusters associated with the particle's track. Therefore, using the Monte Carlo truth, it is possible to see if the clusters used for a tracklet belong to the same particle. If they do not, the tracklet can be labeled as a *fake*. If at least 50% of the tracklets used to reconstruct a vertex are fake, then the reconstructed vertex is also labeled as a fake vertex.

4.1.4 Track reconstruction

A track is the trajectory of a particle through the detector. The basis of track reconstruction is associating the clusters on the different layers to one particle track. This section discusses the outline of the track reconstruction procedure presented in Ref. [48]. Track reconstruction is carried out for ITS+TPC and ITS standalone simultaneously and is,

therefore, not dependent on each other. However, once the reconstruction procedure is completed, the ITS+TPC track may be used to improve the ITS standalone reconstruction. As discussed earlier, for the studies in this thesis, no simulated TPC information was used, i.e., we only use information from the ITS standalone simulation.

Similar to the primary vertex reconstruction, the initial step of reconstructing tracks is identifying tracklets. Furthermore, one defines a window of acceptance for the created tracklets, a window in φ and z. After that, conditions are imposed on the accepted tracklets,

- the difference in φ between the two clusters of a tracklet must be smaller than some chosen limit, $\Delta\varphi < \Delta\varphi_{\mathrm{MAX}}$,
- the DCA_z must be smaller than some chosen limit $\mathrm{DCA}_z^{\mathrm{MAX}}$,

where the DCA_z is the distance of closest approach to the vertex in z. Note again that the bend from the magnetic field affects the $xy - plane$, i.e., particle trajectories correspond to straight lines in z. The DCA is found by prolonging the tracklet and using information from the reconstruction of the primary vertices. An illustration of how tracklets are found is shown in the left part of Fig. 4.1.

The second step is to match the tracklets together to find potential tracks, or track *seeds*, shown in the right part of Fig. 4.1. Once potential tracks are identified, a situation might occur when two potential tracks share one or more clusters. If this is the case, like in the right part of Fig. 4.1, only the track with the lowest χ^2 is kept. The tracks kept are then fitted using a Kalman Filter [49].

Similarly to primary vertex reconstruction, a track may sometimes be labeled as a fake track. A track is considered fake if one or more cluster(s) do not belong to the particle associated with the track according to the Monte Carlo truth information.

4.1.5 Track reconstruction coordinates

To simplify the track reconstruction procedure, a new coordinate system is defined. This new coordinate system is found after a rotation of the transverse plane, with an angle α. The definition of α is in the transverse plane, the angle from the line perpendicular to the tangent of the cluster. In an ideal geometry, this becomes trivial because the track will always be perpendicular to the detector surface, and thus α will coincide with the angle of the track φ.

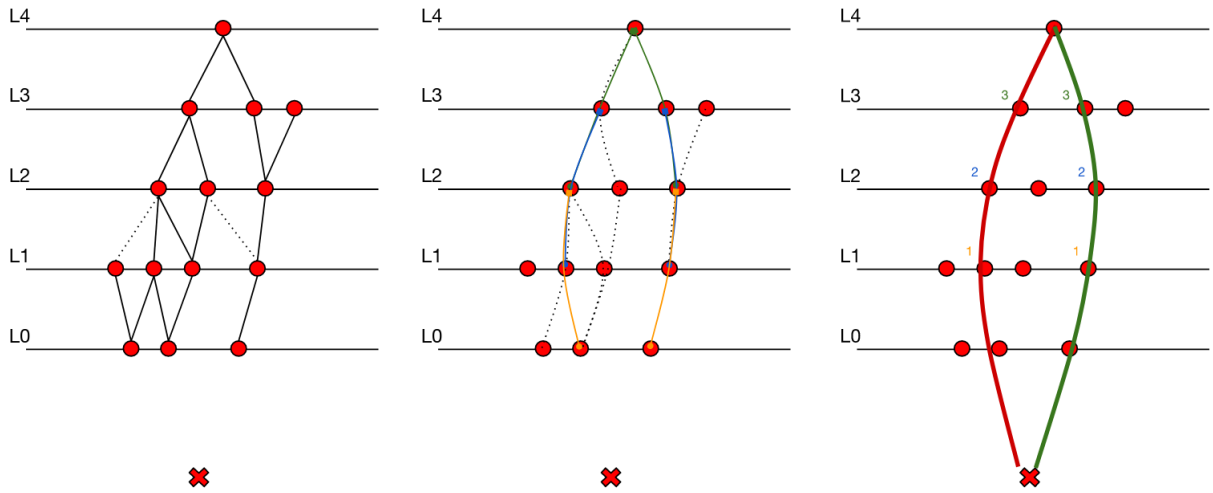

Figure 4.1: Illustrative sketch in the $xy-plane$ of the different steps of track reconstruction that includes tracklet finding (left), matching tracklets (center), and finding of potential track seeds (right). Figure from Ref. [48].

4.2 Definition of performance variables

This section presents the variables used to evaluate the performance of the reconstruction techniques.

4.2.1 Reconstruction efficiency

Primary vertex reconstruction efficiency is the ratio between successfully reconstructed vertices and the total number of vertices. There is one generated vertex per event. The numerator includes fakes because it is only in simulation one can distinguish between good and fake,

$$\varepsilon_v = \frac{N(\text{Events successfully reconstructed})}{N(\text{Total events})}.$$

When it comes to real data, the good and fake vertices are indistinguishable. For that reason, it is also relevant to consider the ratio of fake vertices per event,

$$\varepsilon_v^{fake} = \frac{N(\text{Fake vertices})}{N(\text{Total events})}.$$

For track reconstruction efficiency, we instead define,

$$\varepsilon_t = \frac{N(\text{Good tracks})}{N(\text{Reconstructed tracks})}, \qquad \varepsilon_t^{fake} = \frac{N(\text{Fake tracks})}{N(\text{Reconstructed tracks})}.$$

The definitions of fake vertices, and good and fake tracks were given in Sec. 4.1.3 and 4.1.4 respectively.

4.2.2 Spatial resolution

Several parameters can be evaluated when establishing the track reconstruction performance. First, the previously mentioned DCA is the shortest path between a reconstructed track and the corresponding reconstructed vertex. The DCA values have a Gaussian behavior, which allows one to characterize it using the *resolution*, σ, and the *mean* μ.

Similar to the DCA is the track *residual*, which is the shortest distance from the reconstructed track to the cluster that was used for reconstruction. The residual values also have a Gaussian behavior, leading to the possibility of characterizing the residual distribution in the same way as the DCA.

Lastly, one can examine the accuracy of the reconstructed transverse momentum. This is evaluated using the form,

$$\Delta p_T / p_T^{\text{rec}} = \frac{p_T^{\text{rec}} - p_T^{\text{gen}}}{p_T^{\text{rec}}}, \tag{4.1}$$

which also can be characterized by a Gaussian distribution.

Chapter 5

Procedure

5.1 Modeling distortion

To model the geometry distortion, one should consider many things, such as what a realistic distortion model could be or how strong distortion we should expect. Before addressing these issues, it is essential to understand the effect distortion has on reconstruction.

5.1.1 Distortion transformation

Fig. 5.1 shows a schematic to illustrate the distortion effect. If one considers a particle track in an ideal geometry, as shown in the figure, the pixel on point A would give a signal. By identifying the activated pixel, one can find the global coordinate of the detected hit. However, let us now consider the scenario of a distorted geometry illustrated by the red line. The hit will be detected at point B. By assuming an ideal geometry for reconstruction, when the pixel at point B fires, it would correspond to the estimated position of point C.

The distortion transformation for different models is carried out in the two steps shown in Fig. 5.1. The transformation is done in the global coordinate system described in Sec. 2.5.1, and it is the hits directly after event generation and transportation that are transformed, i.e., before the hits are digitized.

The first step ($A \rightarrow B$) is to *distort* the hits in the ideal geometry (A) and find the distorted coordinate (B). This is done by linearly propagating the hit in the ideal geometry outwards until it intersects the distorted geometry. As tracks are linearly propagated outwards from the origin, the effects of the magnetic field in this step are neglected. The linear propagation from the primary vertex is only valid for primary particles as secondary vertices are displaced with respect to the origin of the coordinate system, which is why only primary particles are considered in this study. An alternate approach was also briefly

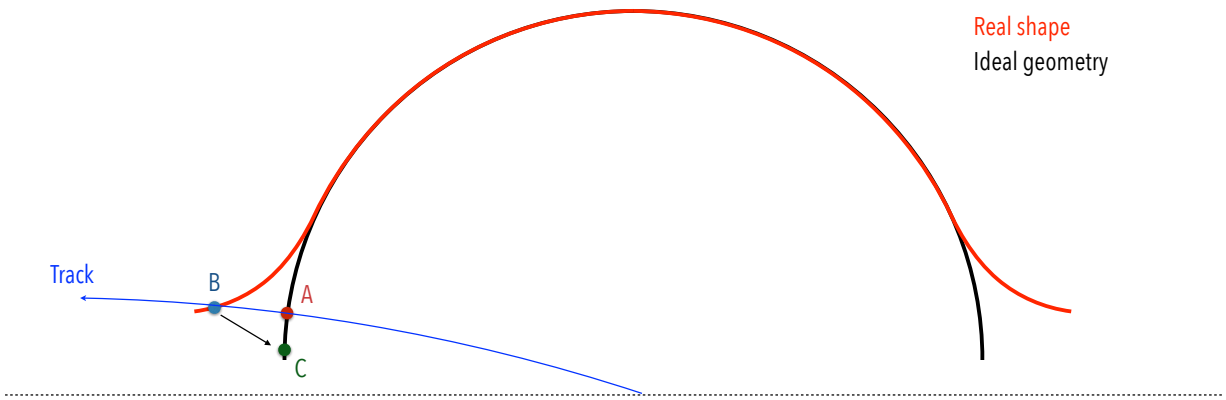

Figure 5.1: Exaggerated illustration of distortion transformation. Point A is a hit that would be measured in an ideal geometry, point B is the actual hit in a distorted geometry, and point C is the measured hit projected back onto the ideal geometry.

investigated where instead of using the hit and origin for the linear propagation, one uses the detector start and end position of a hit[1].

Unique circumstances may arise in distortions. For the distorted geometry example shown in Fig. 5.1, if a hit is close enough to the $x - axis$, it will miss the distorted geometry. These hits are identified and labeled as *misses*. A miss may be identified by the φ angle or the new z coordinate. If the φ angle is not within the azimuthal coverage of the distorted geometry, the hit is labeled as a miss due to φ. If the new z coordinate is beyond the edges of the detector, the hit is labeled as a miss due to z.

Once the initial distortion is done and the distorted coordinate is found, the second step ($B \rightarrow C$) is to *project* the hit back onto the ideal geometry used in the reconstruction. The projection back to the ideal geometry is done by treating both half-layer geometries as curves from the $y - axis$ and computing the arc length from the $y - axis$ to the hit position. Once the arc length to B is found on the distorted curve, it is used to find the position C on the ideal geometry.

After the distortion and projection are finished, a new file is created, overwriting the previously generated one with the new Cartesian coordinates of the hits of the primary particles. Non-primary particles are not altered, and misses are excluded from the new file. The simulation workflow is resumed, where digitization and reconstruction are performed assuming ideal geometry.

[1]In the hit class, every hit has two coordinates, the coordinate for when the particle initially hits the detector (start), and the coordinate for when the particle exits (end).

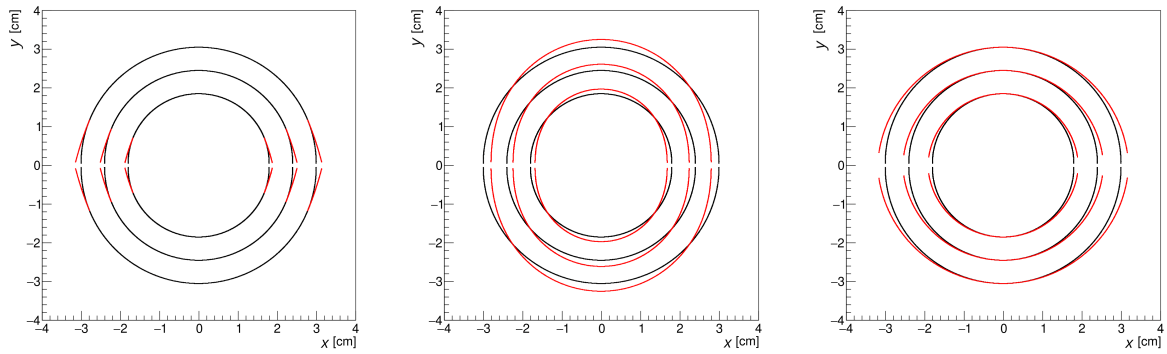

Figure 5.2: Exaggerated distortion models where the default geometry is black, and the distorted geometry is red. Left: quadratic dependence φ introduced on r close to the $x - axis$. Center: elliptical model. Right: radial model.

5.1.2 Studied models

The three studied distortion models are shown in Fig. 5.2. First is a model reminiscent of the one shown in Fig. 5.1. In this model, at some angle from the $y - axis$, a quadratic φ dependence is imposed on the radius, r. This is the only model that is only partially distorted. The second model is an elliptical shape where one could imagine that the detector has been compressed. The third model is a model described as a radial distortion. The radial distortion still has the shape of a cylinder. However, a cylinder with an increased radius centered at a point displaced from the origin such that the points on both the default and distorted geometry at $x = 0$.

To describe the strength of the different types of distortion, a parameter, Δr, is introduced. In the first case, Δr is the closest distance to the ideal geometry from the most distorted hit. In the elliptical model, Δr is,

$$\frac{x^2}{(1+\Delta r)^2} + \frac{y^2}{(1-\Delta r)^2} = 1. \tag{5.1}$$

For the radial model, Δr is the difference in radius between the default and distorted geometry.

5.1.3 Deadzones

As a precautionary matter, in the ITS3 standalone simulation, it is possible to introduce *dead* areas in the detector. A dead area, or zone, is a part of the detector that is not active. The motivation for introducing dead zones is to be able to evaluate detector performance in case further cooling is required to be installed, cable management for read-out electronics,

or simply if some parts stop working. In the case of the distortion transformation, one also has to consider if the projected hit lies in a dead zone. If it does, then the hit must be considered as a miss. Studies of dead zones are an essential part of analyzing physics performance. However, in this work, simulations without dead zones are considered unless explicitly specified. An illustration of the geometry with added dead zones is shown in Fig. A.1.

5.2 Alignment

It was decided to only work with the radial model for the alignment procedure for multiple reasons. First of all, it is considered a realistic model, and unlike the other two models, where some procedures must be done numerically, one can handle the radial model analytically. This drastically reduces computation time, especially when great precision is desired. Secondly, once attempting to extract the distortion parameter from analysis, the procedure becomes more manageable when one can fit a function of only one parameter. Lastly, during alignment, one has to transform the coordinates to the track reconstruction coordinate system discussed in Sec. 4.1.5, which becomes significantly more straightforward using the radial model.

The procedure to be presented was partially based on a similar study at CMS [50]. During the alignment procedure, it is assumed that the type of distortion transformation is known beforehand, but the size of the distortion parameter is not known. Therefore, the task is to implement some method from analysis to extract the distortion parameter and apply a reverse transformation of the clusters before the reconstruction.

5.2.1 Extracting the distortion parameter

Only tracks reconstructed using clusters on all layers are used to find the distortion parameter. It is then possible to find the shortest distance between the track and the cluster that belongs to said track on each layer. We call this quantity the track *residuals*. By considering the track residuals, it is possible to align each layer of the ITS3 independently.

In the left column of Fig. 5.3, the mean of the track residuals for each layer is shown. One can see that there is little to no modulation in the Inner Barrel, and the distortion has a larger effect on layers 3 and 4. This is because the inner layers have more weight than the outer layers in the reconstruction. This distribution of cluster weight between the layers is because particles detected in the Outer Barrel have been more susceptible to multiple scattering than in the Inner Barrel. In other words, the closer to the interaction point, the better the precision of the cluster position.

To extract the distortion parameter, the weight of the Inner Barrel cluster positions is gradually reduced until there is no modulation in the Outer Barrel. The weight is reduced by increasing the positional error of the clusters. Reducing the weight of the inner layer cluster positions makes the outer layers more and more dominant in reconstruction, leading to a stronger modulation in the Inner Barrel. In the right column of Fig. 5.3, the track residuals are shown with a positional uncertainty of 350 µm added to the clusters in the Inner Barrel before reconstruction.

Once the modulation in the Outer Barrel has been reduced and signs of misalignment appear in the Inner Barrel, it is possible to fit a function of one parameter in each layer. The right column of Fig. 5.3 shows a non-continuous behavior in the Inner Barrel; however, the behavior is continuous in each half-layer. The behavior is well-described by a third-degree polynomial, and such a fit is shown in the figure. The third-degree polynomial fitted is defined as,

$$\delta_{xy}(\varphi) = A\varphi^3, \tag{5.2}$$

where A is the fitted parameter. To account for a possible displacement in φ, two different polynomials are fitted,

$$(\delta_{xy})_1(\varphi) = A_1(\varphi - \pi/2)^3, \tag{5.3}$$
$$(\delta_{xy})_2(\varphi) = A_2(\varphi + \pi/2)^3, \tag{5.4}$$

and the parameter A and its associated error, e_A, is found by the average of A_1 and A_2, and propagating the fitted parameter errors e_{A1} and e_{A2},

$$A = \frac{A_1 + A_2}{2} \pm \frac{\sqrt{(e_{A1})^2 + (e_{A2})^2}}{2}. \tag{5.5}$$

The fit parameter A, is then extracted for different distortion parameters ranging from 50 µm to 250 µm, with a step size of 25 µm. Each layer used the same distortion parameter when the fit parameter was extracted. In Fig. 5.4, the correlation between the fit and distortion parameters in the Inner Barrel is shown. As seen in the figure, the correlation is similar across the layers in the Inner Barrel. Furthermore, it is expected that the linear correlation intersects the origin. As for when there is no distortion ($\Delta r = 0$), the fit parameter should be zero because there should be no modulation in any of the layers.

5.2.2 Realigning cluster positions

When the fit parameter has been extracted, a reverse transformation can be applied to the cluster position. If one considers Fig. 5.1, applying the reverse transformation to a cluster on point C moves a new coordinate close to point B, such that the real shape is used for track reconstruction. The procedure of the reverse transformation is similar to the projection from B to C. The arc along the geometry from the $y-axis$ to the cluster point

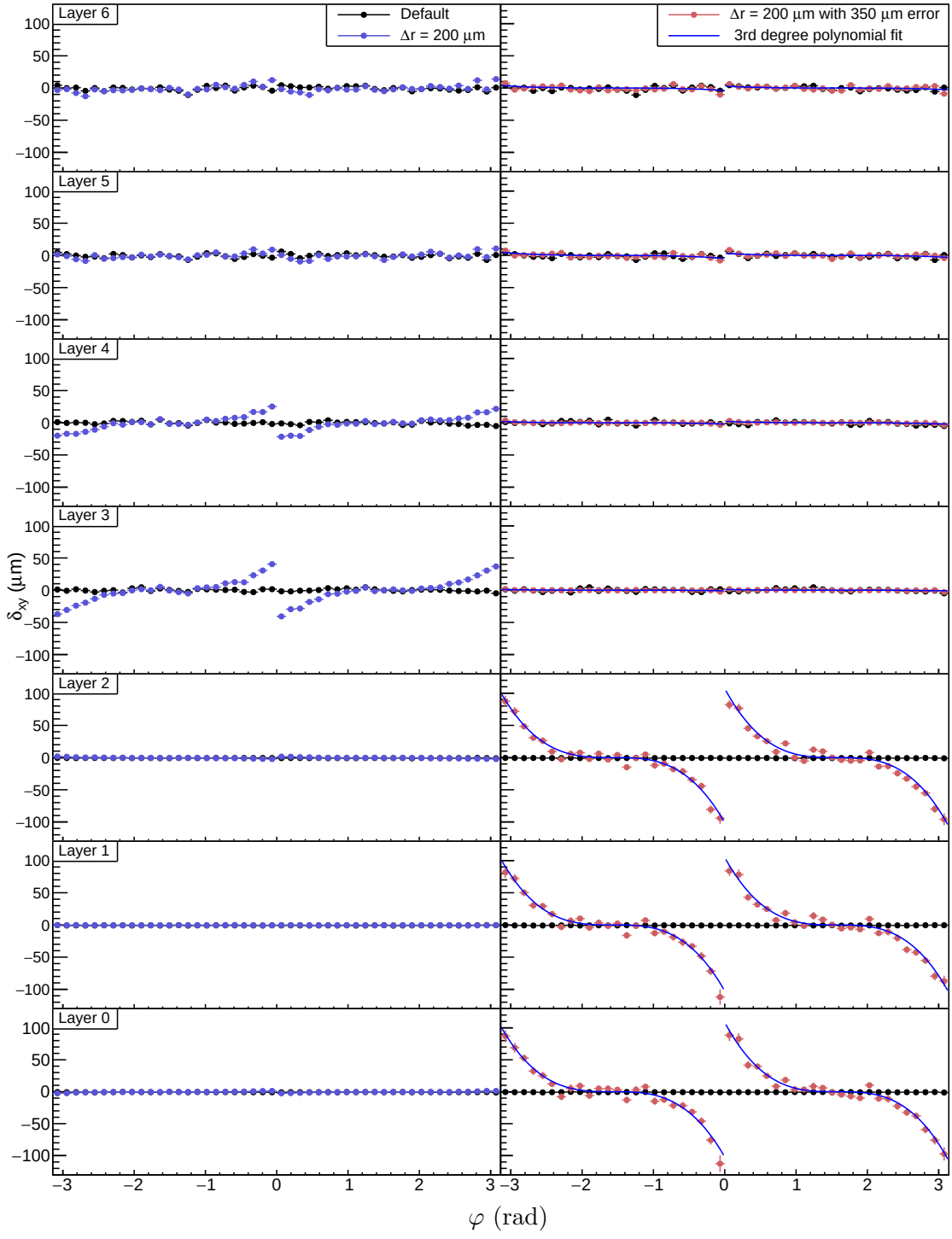

Figure 5.3: Left: track residuals in the transverse plane with an azimuthal dependence in each layer using a distortion parameter of 200 µm. Right: track residuals with an uncertainty of 350 µm added in the Inner Barrel. Each half-layer has also been fitted with a third-degree polynomial.

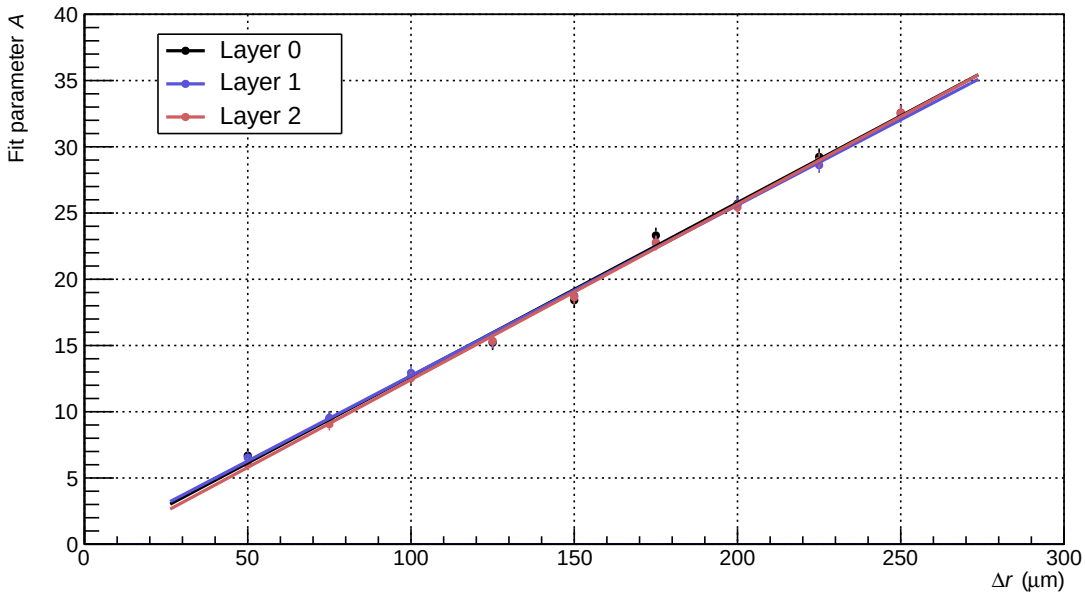

Figure 5.4: Correlation between the fit and distortion parameters in the Inner Barrel.

is computed, and the corresponding position with the same arc length in the geometry distorted by the extracted distortion parameter is then found. As mentioned, the procedure is done independently in each layer, resulting in a slight difference in distortion parameters between the layers in the Inner Barrel.

The reverse transformation is applied to the cluster positions as they are about to be transformed to the track reconstruction coordinates. After the realignment, the transformation is done by finding α, defined in Sec. 4.1.5. Since the radial model is two half-cylinders with a larger radius and their center displaced from the origin, they can be moved using the extracted distortion parameter so that their center coincides with the origin. Then, α coincides with the cluster position's azimuthal angle, φ.

Chapter 6

Results and discussion

6.1 Reconstruction efficiency

6.1.1 Primary vertex reconstruction

In the presence of a distortion uniform across the Inner Barrel, the primary vertex efficiency retains its precision. In Tab. 6.1, performance statistics concerning the primary vertex reconstruction are presented. The ranges of the distortion parameter were selected based on input from mechanical engineers. As discussed in Sec. 5.1.1, this work only considers primary particles. The result is that once the hits are generated in the simulation, hits

Table 6.1: Statistics for reconstructed primary vertices for primary particles in 10^5 simulated events distorted by the radial model.

Distortion parameter (µm)	Usable events(#)	Reconstructed vertices (#)	Fake vertices ε_v^{fake} (%)	Efficiency, ε_v (%)
0	10 000	12 997	0	99.45
25	10 001	13 077	0	99.44
50	10 003	13 054	0	99.25
75	10 000	13 076	0	99.36
100	10 000	13 120	0	99.37
125	10 000	13 123	0	99.43
150	10 000	13 028	0	99.40
175	10 001	13 096	0	99.37
200	10 000	13 051	0	99.48
225	10 000	13 110	0	99.41
250	10 000	13 168	0	99.43

from non-primary particles are excluded during the distortion transformation. This means that digitization and reconstruction only use hits from primary particles. Furthermore, one can see that there are more usable events than simulated events. This is due to the continuous read-out at the ALICE experiment. During reconstruction, one defines ROFs (Read-Out Frames). If an event is at the edge of a ROF, hits from that event will be found in both ROFs, and the simulated vertex will be usable in both ROFs. Thus, the simulated event will be usable twice. This happens also when using only primary particles but occurs more frequently when considering all particles.

In the table, one can also see that the number of reconstructed vertices exceeds the total vertices. This is because a vertex may be reconstructed multiple times from different tracklets without being labeled fake. This, however, does not affect the efficiency as it is defined as vertices successfully reconstructed and not the total number of vertices found. When comparing it to the Monte Carlo truth, one sees that no fake vertices are found, and together with high efficiency, it can be concluded that the selected thresholds in the vertex finding algorithm have been well selected.

Lastly, it is clearly shown in the table that there is no apparent effect of the distortions on vertex efficiency.

6.1.2 Track reconstruction

Tab. 6.2 presents performance statistics concerning track reconstruction. The table shows the efficiency and fake tracks with respect to associated tracks. Furthermore, one can also

Table 6.2: Statistics for reconstructed tracks in 10^5 simulated events distorted by the radial model.

Distortion parameter (µm)	Reconstructed tracks (#)	No associated particle (#)	Fake tracks, ε_t^{fake} (%)	Efficiency, ε_t (%)
0	738 753	7	2.41	97.59
25	745 569	6	2.43	97.57
50	741 839	9	2.41	97.59
75	742 592	8	2.43	97.57
100	745 052	11	2.44	97.56
125	744 623	9	2.46	97.54
150	738 850	8	2.44	97.56
175	741 242	9	2.42	97.58
200	741 192	13	2.45	97.55
225	742 144	13	2.45	97.55
250	745 177	13	2.49	97.51

see the number of tracks with no corresponding particle. These are tracks that have been reconstructed only from noise. It is also clearly apparent from this table that the distortion has no significant effect on the track reconstruction efficiency.

6.2 Distortion parameter

The linear functions from the fit in Fig. 5.3 are found to be,

- Layer 0: $A(\Delta r) = 0.13\Delta r - 0.37$,
- Layer 1: $A(\Delta r) = 0.13\Delta r - 0.68$,
- Layer 2: $A(\Delta r) = 0.13\Delta r - 0.81$.

As a test of the method, for the distortion of $\Delta r = 200\,\mu\text{m}$. Using the inverse of the fitted functions, one can find the distortion parameter for each layer. To separate the extracted distortion parameter from the true value, it is labeled $\Delta r'$. The extracted parameter in each layer was found to be,

- Layer 0: $A = 25.29 \rightarrow \Delta r' = 197.39\,\mu\text{m}$,
- Layer 1: $A = 25.82 \rightarrow \Delta r' = 203.85\,\mu\text{m}$,
- Layer 2: $A = 25.95 \rightarrow \Delta r' = 205.85\,\mu\text{m}$,

Table 6.3: Shows the alignment performance in each layer for several distortion parameters.

Distortion parameter (µm)	Layer 0: $\Delta r'$ (µm)	Layer 1: $\Delta r'$ (µm)	Layer 2: $\Delta r'$ (µm)
25	25.88	29.24	29.94
50	51.40	54.17	59.56
75	72.83	78.96	80.56
100	98.23	102.24	101.48
125	121.50	125.14	124.72
150	145.42	150.51	153.38
175	174.46	178.61	181.82
200	197.39	203.85	205.85
225	228.17	232.99	232.48
250	255.33	261.50	261.53

which gives an indication regarding the precision of the used method. The extracted parameter for other distortions can be seen in Tab. 6.3. It can be seen that the extracted parameter is typically within a few percent of the distortion parameter but can be up to 10 µm off in the worst cases.

6.3 Alignment

This section contains several figures illustrating the track reconstruction performance. In these figures, a cut in pseudorapidity is imposed, $|\eta| < 1$, corresponding to the appropriate acceptance of the ALICE Central Barrel. Tracks must have been reconstructed using all seven layers. Since figures will contain results from the alignment procedure, the distortion model used is the radial model. Furthermore, the distortion parameter used for these figures was $\Delta r = 200\,\mu\text{m}$[1]. The $\Delta r'$ used for realignment are the values presented in the previous section, Sec. 6.2. This section also presents several one-dimensional histograms. These histograms contain the mean, μ, and standard deviation σ of a Gaussian fit to different two-dimensional histograms, containing information such as DCA modulation, spatial and momentum resolution. These histograms can be found in Appendix C, D, and E. They are also referenced in each figure caption.

6.3.1 Distance of Closest Approach modulation

So far, it has been shown that the reconstruction efficiency is not particularly affected by the imposed distortion. However, one starts to see a modulation when considering the DCA of the reconstructed tracks. The red points in Fig. 6.1 show this modulation, and one can see a clear φ dependence, which is to be expected due to the φ dependence of the distortion. In the transverse plane (xy), this is a similar modulation to the one in the Inner Barrel in the right part of Fig. 5.3. In the beam direction (z), it can be seen that there is no significant change due to the distortion, except for slight anomalies at the edges of the half-layers ($[0, \pi]$ and $[-\pi, 0]$).

Once the clusters have been realigned, one can see from the blue points in Fig. 6.1 that the modulation of $\mu(\text{DCA}_{\text{xy}})$ is greatly reduced. It is not reduced to the point where it would be identical to the default simulation. However, the majority of what is lost in performance is recovered. In the direction along the beam axis, the minor anomalies at the edges of the half-layers $\mu(\text{DCA}_{\text{z}})$ are fully restored.

If one instead are to consider the $\mu(\text{DCA})$ with respect to the generated p_T, one sees a different behavior (see Fig. 6.2). In the top part of the figure, we see $\mu(\text{DCA}_{\text{xy}})$, and in the bottom part, $\mu(\text{DCA}_{\text{z}})$. The first bin in these histograms are tracks with p_T less than $100\,\text{MeV/c}$, and what can be seen is that the statistical uncertainty in this bin is significantly higher than the other ones. Thus, there is no obvious worsening or improvement to the $\mu(\text{DCA})$. In the p_T range up to $1\,\text{GeV/c}$, there is little to no modulation due to the distortion. It is not until the p_T is higher than $1\,\text{GeV/c}$ that the modulation in both xy

[1] A larger value of the distortion parameter was selected for this section to illustrate the distortion effects more clearly. However, input from mechanical engineers suggests that a distortion parameter of 50 µm is more realistic. Therefore, the same figures presented in this section will also be included in Appendix B where instead a distortion of 50 µm was used.

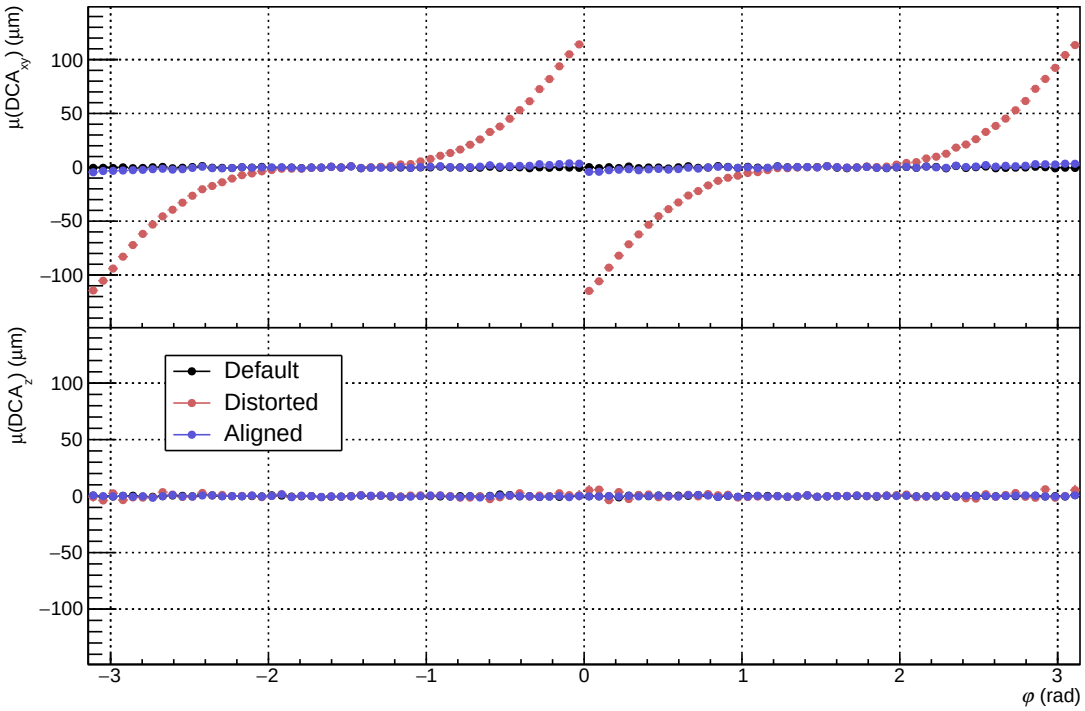

Figure 6.1: The mean of the DCA versus the azimuthal angle, both in x & y and z for tracks from the default simulation, together with distorted and realigned tracks. Projections created from the histograms in Appendix C, Fig. C.1.

and z appears. However, it can be seen that the realignment procedure works well in the higher momentum region, and the modulation vanishes.

6.3.2 Spatial resolution

To further examine the performance loss due to the distortion and the performance recovery, one can look at the standard deviation, σ, of the Gaussian fitted to the μ(DCA) to further examine the performance loss due to the distortion and the performance recovery. One commonly refers to this quantity as the spatial resolution since it is a parameter that directly describes the precision of the track reconstruction.

If one were to consider the $\sigma(\mathrm{DCA_{xy}})$ vs φ, there is no noticeable difference between the default and distorted simulations. For the $\sigma(\mathrm{DCA_z})$, one sees a gradual increase from the center of the half-layer to the edges. This can be seen in the top panel of Fig. 6.3. The alignment brings the $\sigma(\mathrm{DCA_z})$ values back to the default (undistorted) values.

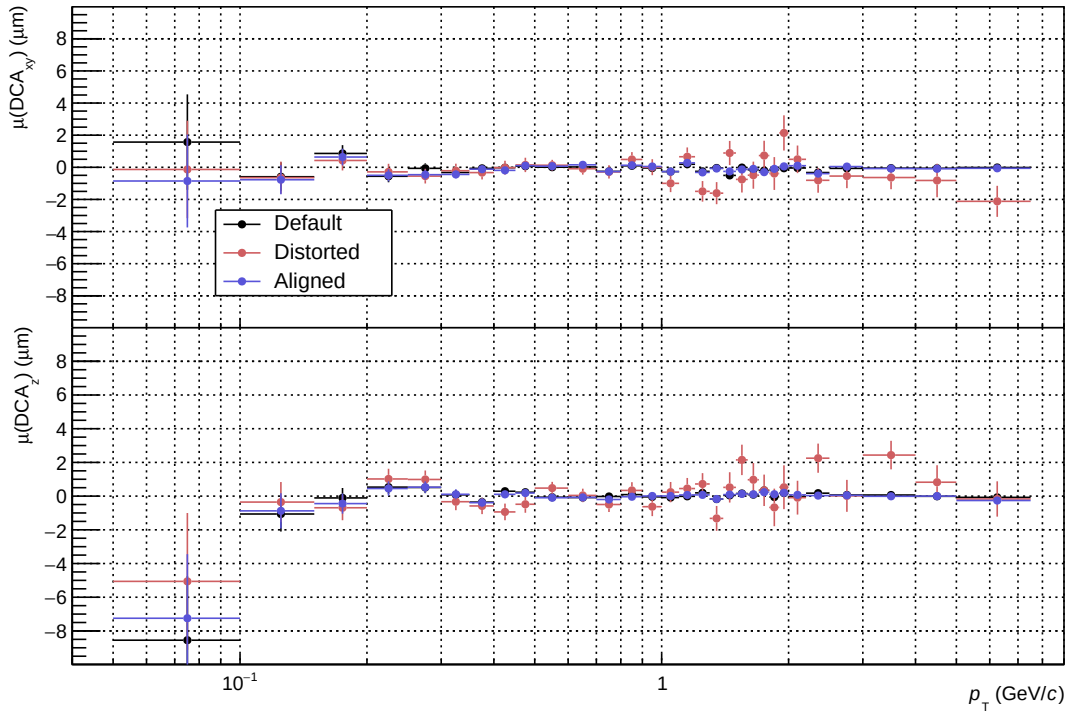

Figure 6.2: The mean of the DCA versus the generated p_T, both in x & y and z for tracks from the default simulation, together with distorted and realigned tracks. Projections created from histograms in Appendix C, Fig C.2.

In the bottom panel of Fig. 6.3, one can, first of all, see how the spatial resolution improves as the p_T increases in the default simulations (black points). This figure demonstrates the performance loss regarding spatial resolution, due to the applied distortion, worsens significantly for higher momentum particles, and this is the case for both $\sigma(\mathrm{DCA_{xy}})$ and $\sigma(\mathrm{DCA_z})$. After applying the alignment procedure, as seen in the figure, the original performance is regained to the point where it becomes difficult to distinguish the points from the default simulation (black) from the realigned points (blue).

6.3.3 Positive and negative tracks

In Sec. 5.1.1, it was discussed that for the distortion transformation, tracks were propagated linearly, and thus the effects of the magnetic field are neglected. To confirm that this approximation is acceptable, one can look at the difference in $\mu(\mathrm{DCA})$ between positively and negatively charged tracks. This is presented in Fig. 6.4 and as shown, there is no significant difference in either $\mu(\mathrm{DCA_{xy}})$ or $\mu(\mathrm{DCA_z})$, which supports that the approximation made is valid.

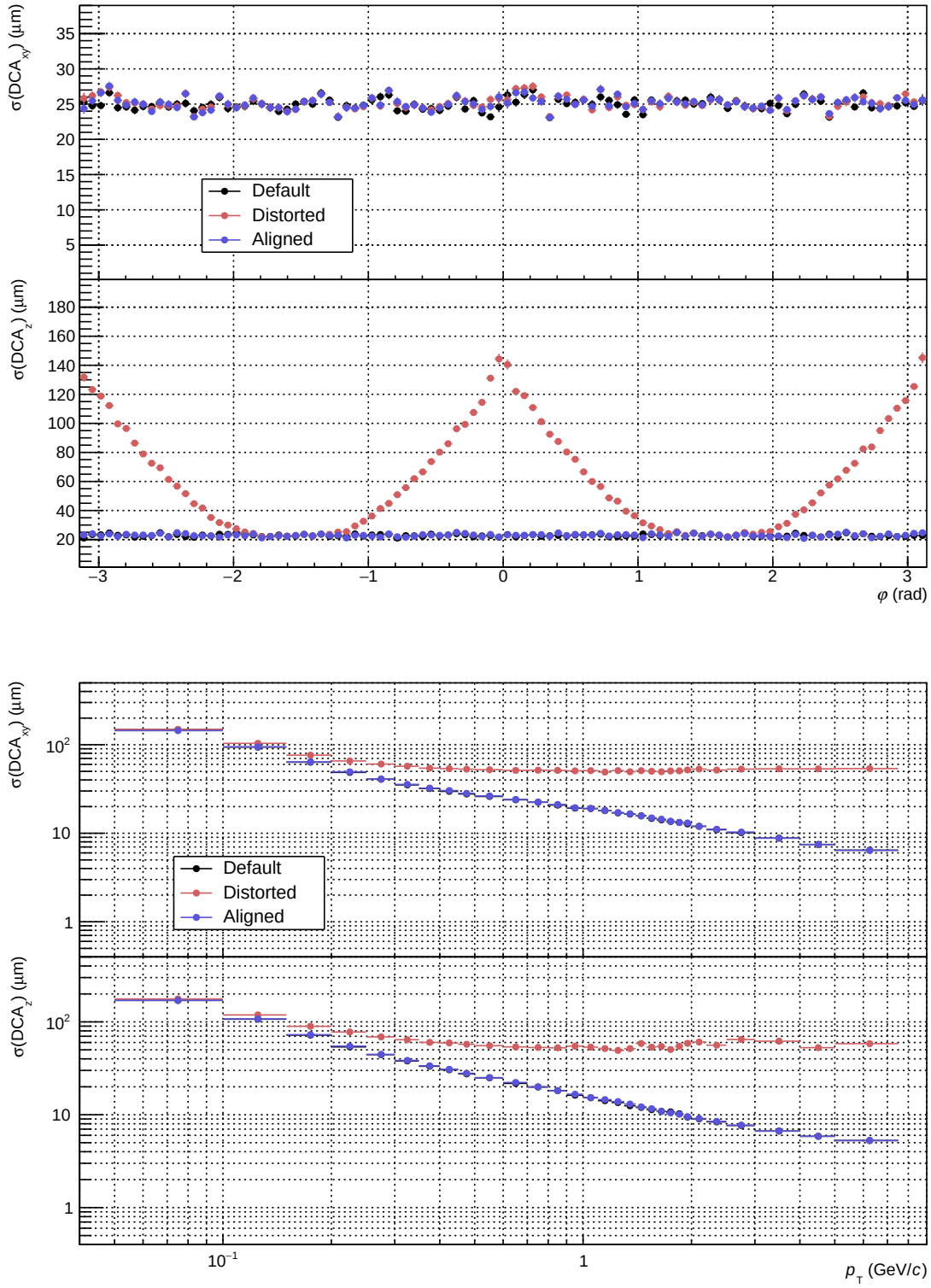

Figure 6.3: σ(DCA) versus φ (top), and versus the generated p_T (bottom) for tracks from the default simulation, together with distorted and realigned tracks. Projections created from histograms in Appendix C, Fig C.1 and C.2.

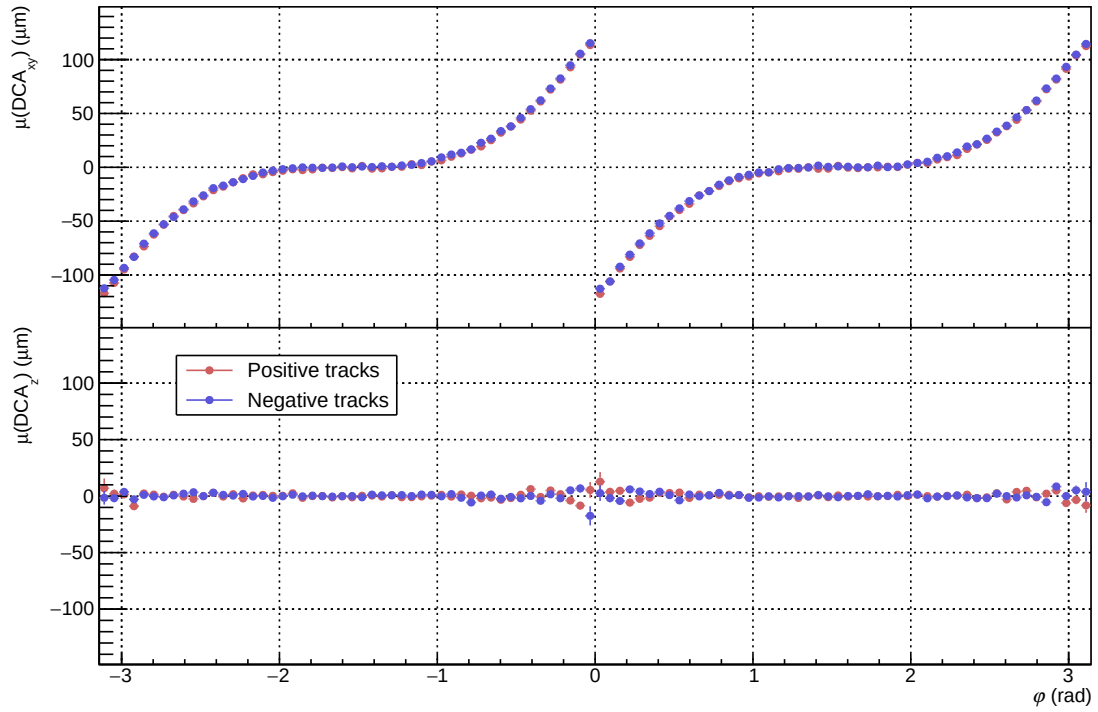

Figure 6.4: The difference in the mean of the DCA versus the azimuthal angle, both in x & y and z for distorted positive and negative tracks. Projections created from histograms in Appendix D, Fig D.1 and D.2.

6.3.4 Difference between transformations

To understand the difference between the different distortion transformation methods mentioned earlier, we consider the difference of how the alignment procedure performs. These transformations either use the hit position and origin (origin to start or origin to end) or the start and end positions of the hit for the linear propagation used for the deformation transformation. These two methods yield different results when evaluating the reconstruction performance. If one considers Fig. 6.5, the difference in spatial resolution is shown for both methods, and one can see that for $\sigma(\mathrm{DCA_{xy}})$, the spatial resolution of the start-to-end method is worse than for the distortion using the origin-to-hit method. Furthermore, we know from the top part of Fig. 6.3 that the aligned tracks using the origin-to-hit method recover the original performance, and one can see that after aligning the tracks that have been distorted using the start-to-end hits, we do not recover much of the lost performance. The performance after alignment, when using start-to-end hits, is worse than the performance after origin-to-hit deformation.

However, the $\sigma(\mathrm{DCA_z})$ have the same effect for both methods and in both cases, one

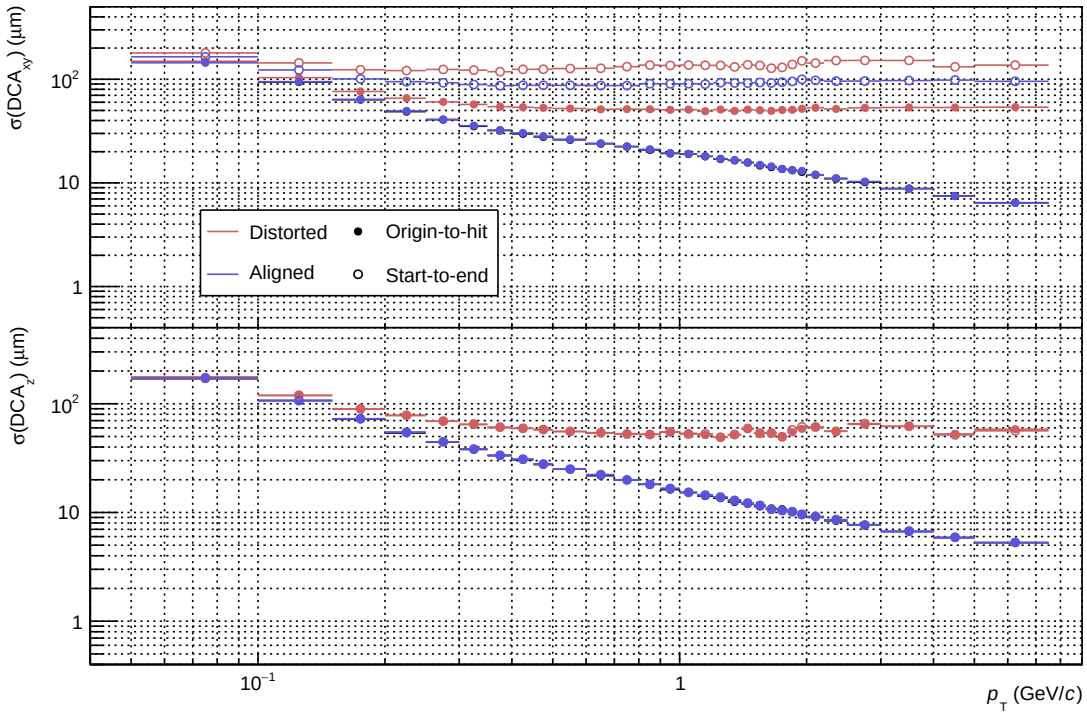

Figure 6.5: σ(DCA) versus the generated and versus φ for distorted and realigned tracks using two different methods for the distortion transformation.

is fully able to recover the original performance.

6.3.5 Momentum resolution

Another topic of interest is the effect that the distortion has on the reconstructed momentum. In Fig. 6.6, both $\mu(\Delta p_T/p_T)$ (top) and $\sigma(\Delta p_T/p_T)$ (bottom) are shown with respect to generated momentum. In the top part of the figure, one can see that the default simulation (black points) overlaps perfectly with the distorted (red points) and aligned (blue points) simulation. Therefore, it can be concluded that the distortion does not introduce any modulation to the mean of the reconstructed momentum. However, if one instead considers the momentum resolution in the bottom part of Fig. 6.6, one sees that there is a minor increase in momentum resolution for higher momentum.

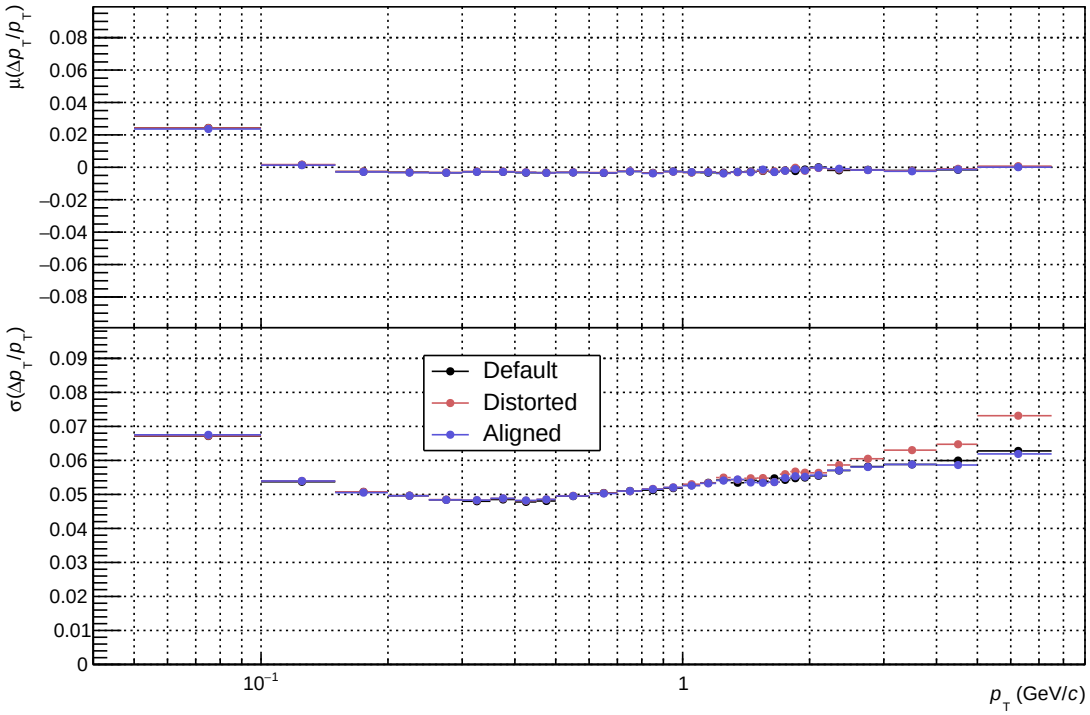

Figure 6.6: Shows $\mu(\Delta p_T/p_T)$ and $\sigma(\Delta p_T/p_T)$ versus generated p_T, both in x & y and z for tracks from the default simulation, together with distorted and realigned tracks. Projections created from histograms in Appendix E, Fig E.1.

6.4 Distortion effects summary

From what has been presented in this chapter, it can be concluded that a mechanical distortion does not necessarily affect the reconstruction efficiency but instead introduces a modulation in the μ(DCA) with φ and p_T dependence. In φ the distortion introduces a modulation in $\mu(\mathrm{DCA_{xy}})$ (see Fig. 6.1). Using a distortion parameter of $\Delta r = 200\,\mu\mathrm{m}$ gives a modulation of up to 100 µm. Despite this modulation, the spatial resolution, $\sigma(\mathrm{DCA_{xy}})$, retains its performance in the transverse plane. Unlike $\mathrm{DCA_z}$, where there is no modulation of $\mu(\mathrm{DCA_{xy}})$, but a significant increase in spatial resolution, $\sigma(\mathrm{DCA_z})$, towards the edges in the half-barrels (see bottom panel of Fig. 6.3).

If one instead considers the modulation of the φ integrated performance, μ(DCA) versus p_T (see Fig. 6.2), one sees a modulation appearing for $p_T < 1\,\mathrm{GeV/c}$ in both $\mu(\mathrm{DCA_{xy}})$ and $\mu(\mathrm{DCA_z})$. Unlike in φ, the modulation in this case does not show any particular pattern but instead is seemingly randomly distributed around $\mu(\mathrm{DCA}) = 0$. This is likely due to the broad distribution for higher p_T, illustrated by the significant increase in σ(DCA), shown in the top panel in Fig. 6.3.

6.5 Alignment performance summary

The realignment procedure generally recovers the performance lost due to mechanical distortions. The exception is $\mu(\mathrm{DCA_{xy}})$ versus φ where one can still see a minimal modulation (see Fig. 6.1). Otherwise, if one considers the figures of $\sigma(\mathrm{DCA})$ or $(\Delta p_T/p_T)$, one finds that the aligned histogram almost always perfectly coincides with the default simulation.

Chapter 7

Conclusion and outlook

7.1 Summary

To conclude, this thesis focused on modeling mechanical distortions in simulations of the inner tracker upgrade at the ALICE experiment. Methods for transforming the ideal geometry into a distorted one were developed and presented. The vertex and track reconstruction efficiency was then evaluated and compared to the same results for an ideal geometry. Furthermore, the DCA's behavior was investigated in terms of mean and spatial resolution. It was found that mechanical distortions do not significantly affect efficiency. However, it results in modulations appearing in μ(DCA) and a degradation in spatial resolution. One could also see a minor degradation of the momentum resolution for higher p_T.

Furthermore, a strategy was developed and presented to extract the parametrization for the distortion such that one can perform a reverse transformation to the distortion, thus allowing one to realign the distorted geometry. This reverse transformation was implemented in the O^2 framework to "on-the-fly" realign clusters used for the track reconstruction. Performance variables were then investigated again so that one could evaluate the performance of the realignment.

It was found that using this strategy, it was possible to regain the performance lost due to mechanical distortions, both in terms of the mean DCA distribution and spatial resolution. It was also possible to regain the precision of the momentum resolution at higher p_T after realignment.

The results of these studies are included in the ITS3 Technical Design Report, which will be made public in the coming months.

7.2 Further alignment studies

In this work, three different proposed distortion models were considered, and due to the computational simplicity of the radial model, it was possible to develop a reverse transformation unique to that model. A course of future work would be to develop a more efficient general reverse transformation and a general transformation from global to tracking coordinates.

The extracted distortion parameter in this work was always within 5 µm, which resulted in successfully recovering the lost performance. This is the same order as the detector's expected position resolution (pixel pitch/$\sqrt{12}$). It would be interesting to investigate the required accuracy of the distortion parameter extraction.

It would also be interesting to look into the effects of having different distortion parameters in each layer or even different distortion transformations entirely.

7.3 Alignment using Millipede

Previous iterations of the alignment procedure were performed using the Millipede algorithm [51] to minimize the χ^2 of the track residuals. By this alignment method, one is not required to know the distortion transformation to perform alignment, which is needed for the work presented in this thesis. Therefore, a further development of this study would be to attempt to implement and perform alignment using the Millipede algorithm.

References

[1]W. N. Cottingham and D. A. Greenwood, *An Introduction to the Standard Model of Particle Physics*, 2nd ed. (Cambridge University Press, 2007).

[2]P. W. Higgs, "Broken symmetries and the masses of gauge bosons", Phys. Rev. Lett. **13**, 508–509 (1964).

[3]G. Aad et al., "Observation of a new particle in the search for the Standard Model Higgs boson with the ATLAS detector at the LHC", Physics Letters B **716**, 1–29 (2012).

[4]S. Chatrchyan et al., "Observation of a new boson at a mass of 125 GeV with the CMS experiment at the LHC", Physics Letters B **716**, 30–61 (2012).

[5]The ALICE Collaboration, "The ALICE experiment at the CERN LHC", Journal of Instrumentation **3**, S08002 (2008).

[6]CERN, *ALICE*, Accessed September 2023, https://home.cern/science/experiments/alice.

[7]ALICE Collaboration, *ALICE O^2 Project*, Accessed May 2023, (2018) https://alice-o2-project.web.cern.ch/.

[8]D. Chandler, *Introduction to modern statistical mechanics* (Oxford University Press, 1987), pp. 89–97.

[9]C. Burgard and D. Galbraith, *Example: Standard model of physics*, Accessed September 2023, https://texample.net/tikz/examples/model-physics/.

[10]H. Spinelli, *Bosons-Hadrons-Fermions-RGB-Diagram*, Accessed October 2023, https://commons.wikimedia.org/wiki/File:Bosons-Hadrons-Fermions-RGB.svg.

[11]C. Gale, J.-F. Paquet, B. Schenke, and C. Shen, "Probing Early-Time Dynamics and Quark-Gluon Plasma Transport Properties with Photons and Hadrons", Nuclear Physics A **1005**, The 28th International Conference on Ultra-relativistic Nucleus-Nucleus Collisions: Quark Matter 2019, 121863 (2021).

[12]J. Adam et al., "Enhanced production of multi-strange hadrons in high-multiplicity proton–proton collisions", Nature Physics **13**, 535–539 (2017).

[13]N. Herrmann, J. P. Wessels, and T. Wienold, "Collective flow in heavy-ion collisions", Annual Review of Nuclear and Particle Science **49**, 581–632 (1999).

[14]A. Lechner, "Particle interactions with matter", CERN Yellow Rep. School Proc. **5**, 47 (2018).

[15]W. T. Scott, "The theory of small-angle multiple scattering of fast charged particles", Rev. Mod. Phys. **35**, 231–313 (1963).

[16]W. Poonsawat, C. Kobdaj, M. Sitta, and Y. Yan (ALICE), *Material Budget Calculation of the new Inner Tracking System, ALICE. Material Budget Calculation of the new Inner Tracking System, ALICE, Tech Report*, 2017.

[17]B. Shaw and B.R. Martin, *Particle physics* (John Wiley & Sons, 2008), pp. 85–86.

[18]ALICE Collaboration, *Definition of the ALICE Coordinate System and Basic Rules for Sub-detector Components Numbering*, Accessed October 2023, (2003) https://alice-servotech.web.cern.ch/HELP_DCDB-SVT/Help_Files/ALICE-INT-2003-038.pdf.

[19]CERN, Accessed September 2023, https://www.home.cern/science/accelerators/large-hadron-collider.

[20]The ATLAS Collaboration, "The ATLAS Experiment at the CERN Large Hadron Collider", Journal of Instrumentation **3**, S08003 (2008).

[21]The CMS Collaboration, "The CMS experiment at the CERN LHC", Journal of Instrumentation **3**, S08004 (2008).

[22]The LHCb Collaboration, "The LHCb Detector at the LHC", Journal of Instrumentation **3**, S08005 (2008).

[23]D. Saikumar, "Future of computing at the Large Hadron Collider", 10.48550/arXiv.2210.13213 (2022).

[24]CERN, *ATLAS*, Accessed September 2023, https://home.cern/science/experiments/atlas.

[25]CERN, *CMS*, Accessed September 2023, https://home.cern/science/experiments/cms.

[26]CERN, *LHCb*, Accessed September 2023, https://home.cern/science/experiments/lhcb.

[27]A. Tauro, *ALICE Schematics*, General Photo, (2017)

[28]B. Abelev et al. (ALICE), *Technical Design Report for the Upgrade of the ALICE Inner Tracking System, Tech Rep*, 2014.

[29]C. Zampolli, *Particle Identification with the ALICE detector at the LHC*, 2012.

[30]P. Kuijer, "The inner tracking system of the Alice experiment", Nuclear Instruments and Methods in Physics Research Section A: Accelerators, Spectrometers, Detectors and Associated Equipment **530**, Proceedings of the 6th International Conference on Large Scale Applications and Radiation Hardness of Semiconductor Detectors, 28–32 (2004).

[31]*ALICE Inner Tracking System (ITS): Technical Design Report*, Technical design report. ALICE (CERN, Geneva, 1999).

[32]M. Mager, "ALPIDE, the Monolithic Active Pixel Sensor for the ALICE ITS upgrade", Nuclear Instruments and Methods in Physics Research Section A: Accelerators, Spectrometers, Detectors and Associated Equipment **824**, Frontier Detectors for Frontier Physics: Proceedings of the 13th Pisa Meeting on Advanced Detectors, 434–438 (2016).

[33]F. Reidt, "Upgrade of the ALICE ITS detector", Nuclear Instruments and Methods in Physics Research Section A: Accelerators, Spectrometers, Detectors and Associated Equipment **1032**, 166632 (2022).

[34]F. Reidt, *Upgrading the Inner Tracking System and the Time Projection Chamber of ALICE*, (Feb. 2020)

[35]*Expression of Interest for an ALICE ITS Upgrade in LS3*, (2018) https://cds.cern.ch/record/2644611.

[36]P. V. Leitao et al., "Development of a Stitched Monolithic Pixel Sensor prototype (MOSS chip) towards the ITS3 upgrade of the ALICE Inner Tracking system", Journal of Instrumentation **18**, C01044 (2023).

[37]E. Biolcati, "Measurement of identified charged hadron spectra in proton-proton collisions using the Inner Tracking System of the ALICE experiment at the LHC", **1343**, 10.1063/1.3575069 (2011).

[38]S. Beolè, "The ALICE Inner Tracking System: Performance with Proton and Lead Beams", Physics Procedia **37**, Proceedings of the 2nd International Conference on Technology and Instrumentation in Particle Physics (TIPP 2011), 1062–1069 (2012).

[39]*Upgrade of the ALICE Time Projection Chamber*, tech. rep. (2013).

[40]C. Lippmann, "Performance of the alice time projection chamber", Physics Procedia **37**, Proceedings of the 2nd International Conference on Technology and Instrumentation in Particle Physics (TIPP 2011), 434–441 (2012).

[41]G. Dellacasa et al. (ALICE), *ALICE Time Projection Chamber: Technical Design Report*, Technical design report. ALICE (CERN, Geneva, 2000).

[42]I. Antcheva et al., "ROOT - A C++ framework for PetaByte data storage, statistical analysis and visualization", Computer Physics Communications **180**, 2499–2512 (2009).

[43]D. D. Chinellato et al., *O2 Analysis Tutorial 2.0*, (2023) https://indico.cern.ch/event/1267433/timetable/#20230417.

[44]C. Bierlich, S. Chakraborty, N. Desai, et al., *A comprehensive guide to the physics and usage of PYTHIA 8.3*, 2022.

[45]Accesed November 2023, https://www.pythia.org/latest-manual/PhaseSpaceCuts.html.

[46]S. Agostinelli, J. Allison, K. Amako, et al., "Geant4—a simulation toolkit", Nuclear Instruments and Methods in Physics Research Section A: Accelerators, Spectrometers, Detectors and Associated Equipment **506**, 250–303 (2003).

[47]M. Concas, "Primary vertex reconstruction using GPUs for the upgrade of the Inner Tracking System of the ALICE experiment at LHC", PhD thesis (Politecnico Di Torino, Sept. 2020).

[48]M. Puccio, "Study of the production of nuclei and anti-nuclei at the LHC with the ALICE experiment", PhD thesis (Università degli studi di Torino, May 2017).

[49]R. Frühwirth, "Application of Kalman filtering to track and vertex fitting", Nuclear Instruments and Methods in Physics Research Section A: Accelerators, Spectrometers, Detectors and Associated Equipment **262**, 444–450 (1987).

[50]"Strategies and performance of the CMS silicon tracker alignment during LHC Run 2", Nuclear Instruments and Methods in Physics Research Section A: Accelerators, Spectrometers, Detectors and Associated Equipment **1037**, 166795 (2022).

[51]V. Blobel and C. Kleinwort, *A new method for the high-precision alignment of track detectors*, 2002.

Appendix

A ITS3 geometry with dead zones

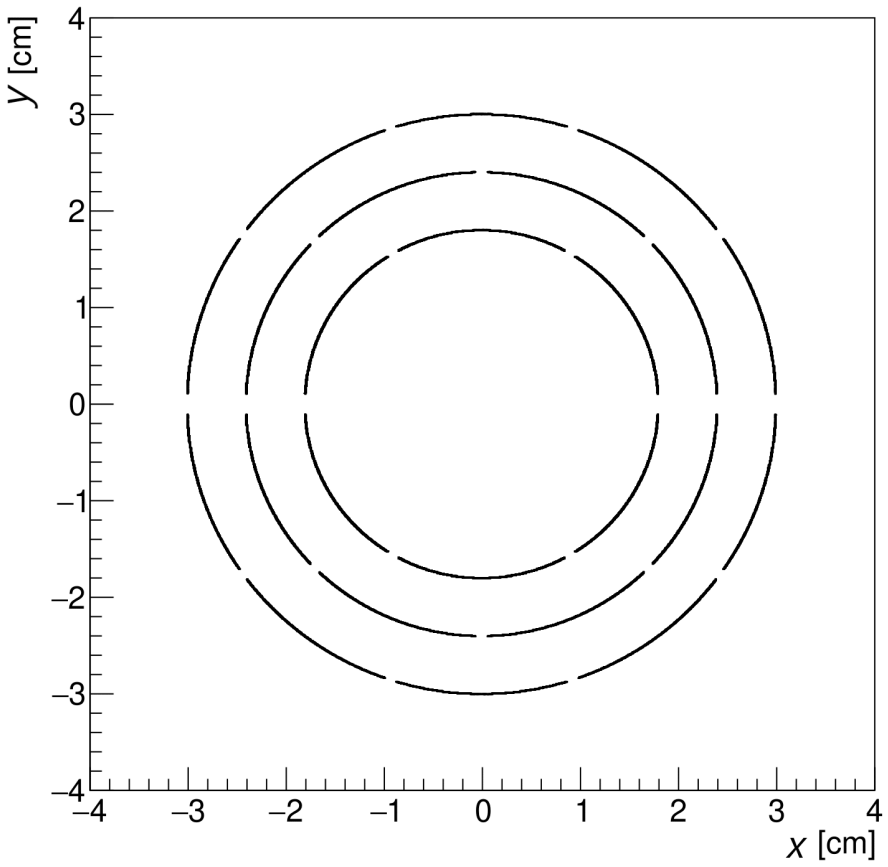

Figure A.1: Default ITS3 simulation, when including dead zones in the detector.

B Distortion and alignment for a distortion parameter of 50 μm

This appendix presents the same figures that have been shown in Sec. 6.3, but instead of a distortion parameter of 200 µm, a smaller, more realistic distortion of 50 µm was used. The extracted parameters used for realignment are found in Tab. 6.3. These histograms are also projections of two-dimensional histograms, but those are not included here. If the reader would like to get an idea about these two-dimensional histograms, please consider the case of 200 µm, where the two-dimensional histograms are included in Appendix C, D and E.

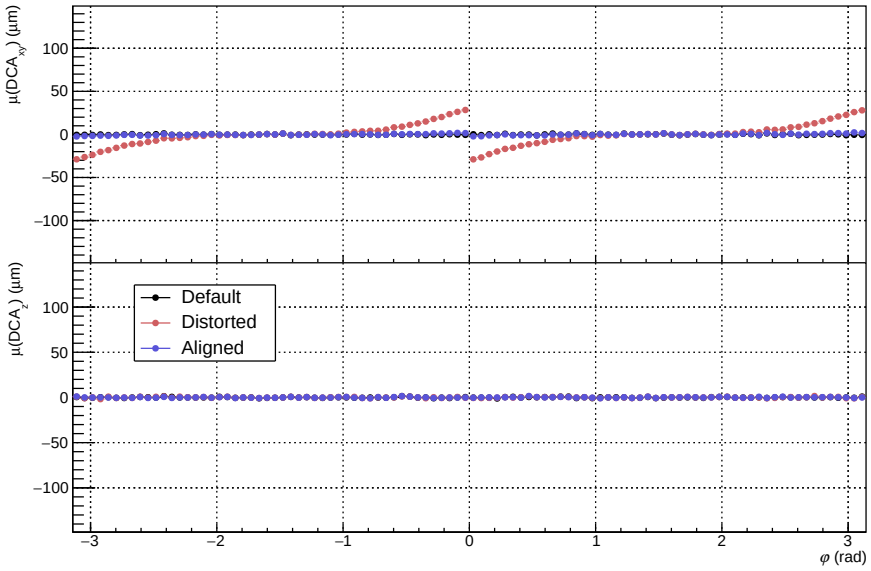

Figure B.1: The mean of the DCA versus the azimuthal angle, both in x & y and z for default, distorted, and realigned tracks.

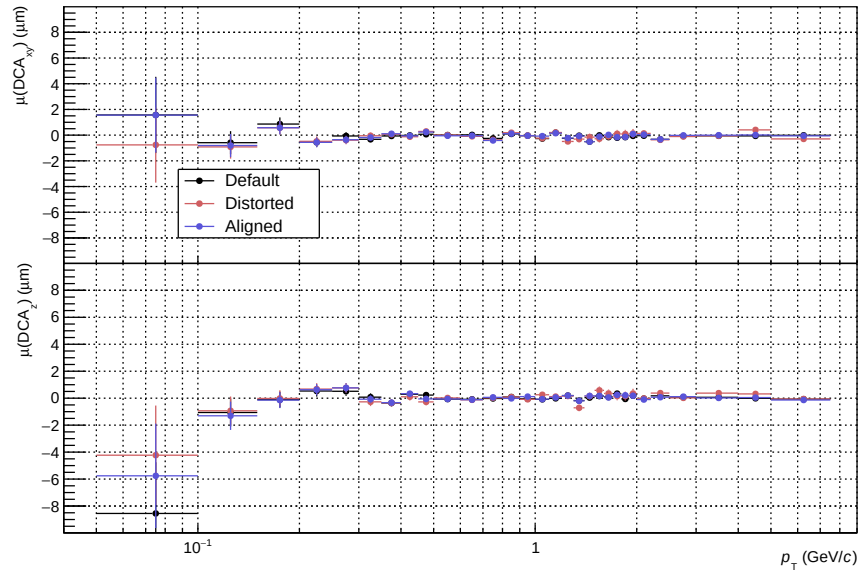

Figure B.2: The mean of the DCA versus the generated p_T, both in x & y and z for default, distorted, and realigned tracks.

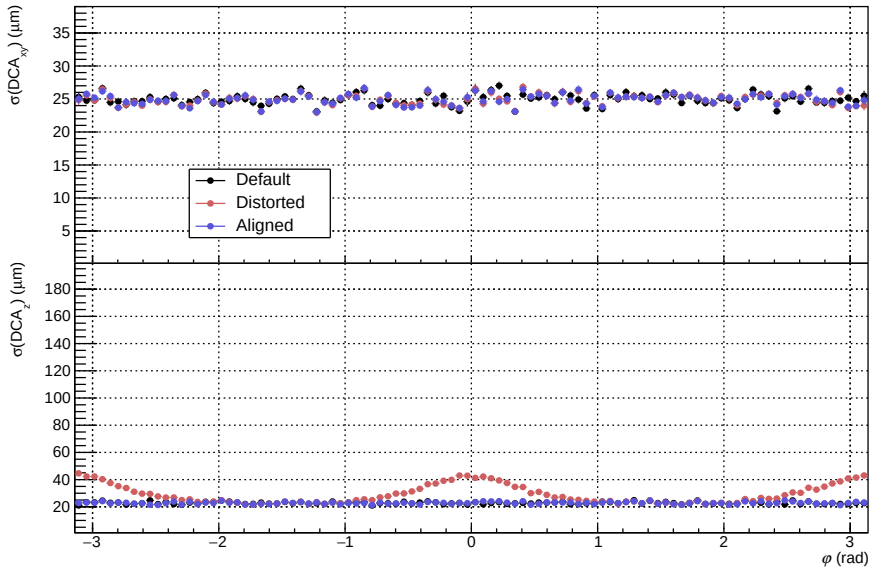

Figure B.3: σ(DCA) versus φ for default, distorted, and realigned tracks.

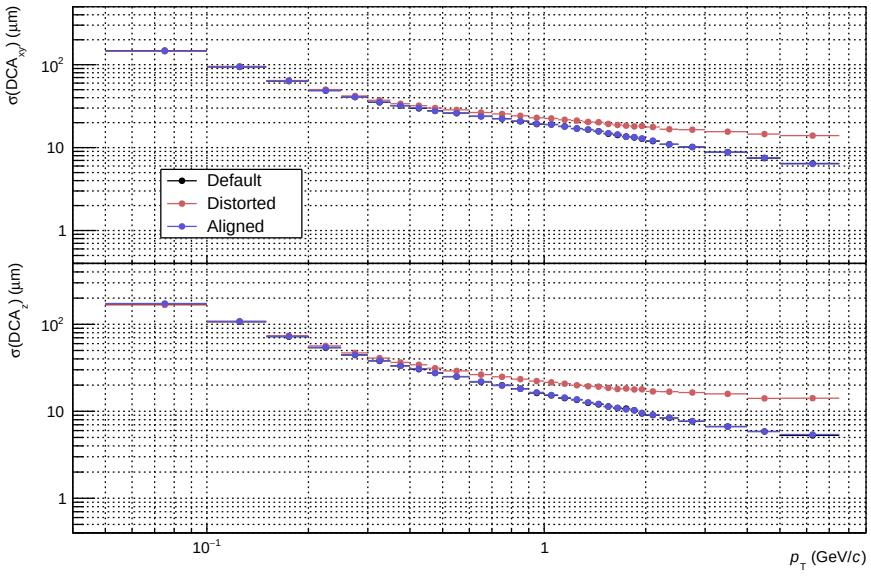

Figure B.4: σ(DCA) versus p_T for default, distorted, and realigned tracks.

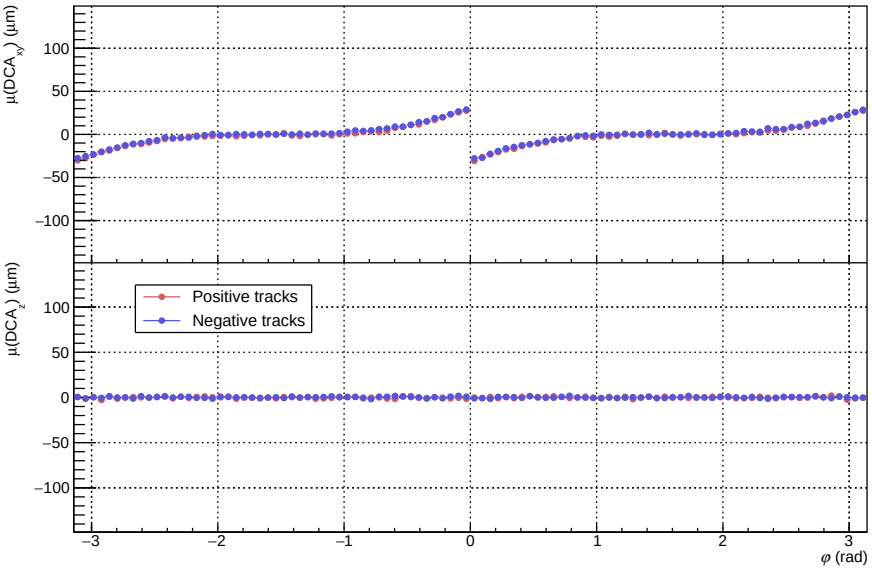

Figure B.5: The difference in the mean of the DCA versus the azimuthal angle, both in x & y and z for distorted positive and negative tracks.

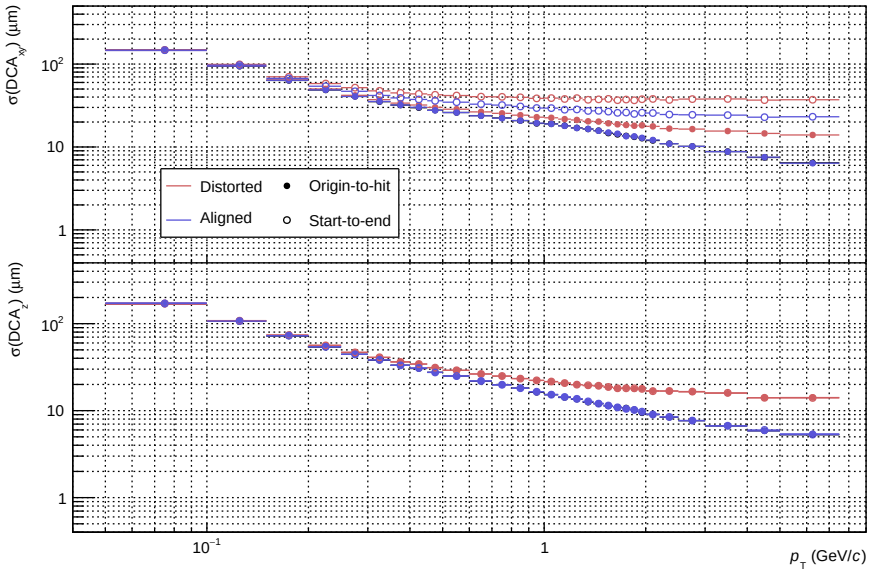

Figure B.6: σ(DCA) versus the generated and versus φ for distorted and realigned tracks using two different methods for the distortion transformation.

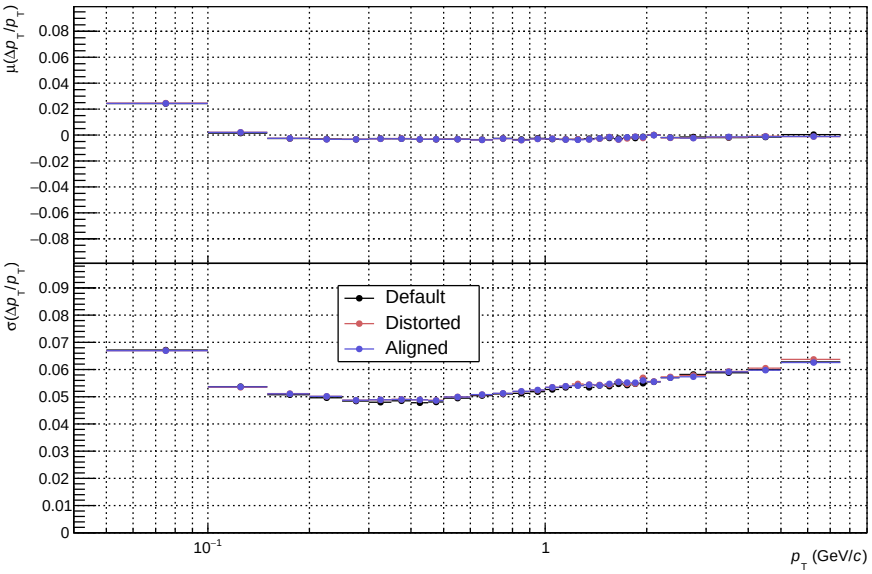

Figure B.7: Shows $\mu(\Delta p_T/p_T)$ and $\sigma(\Delta p_T/p_T)$ versus generated p_T, both in x & y and z for tracks from the default simulation, together with distorted and realigned tracks.

C Two-dimensional histograms of the DCA versus generated p_T, and versus φ

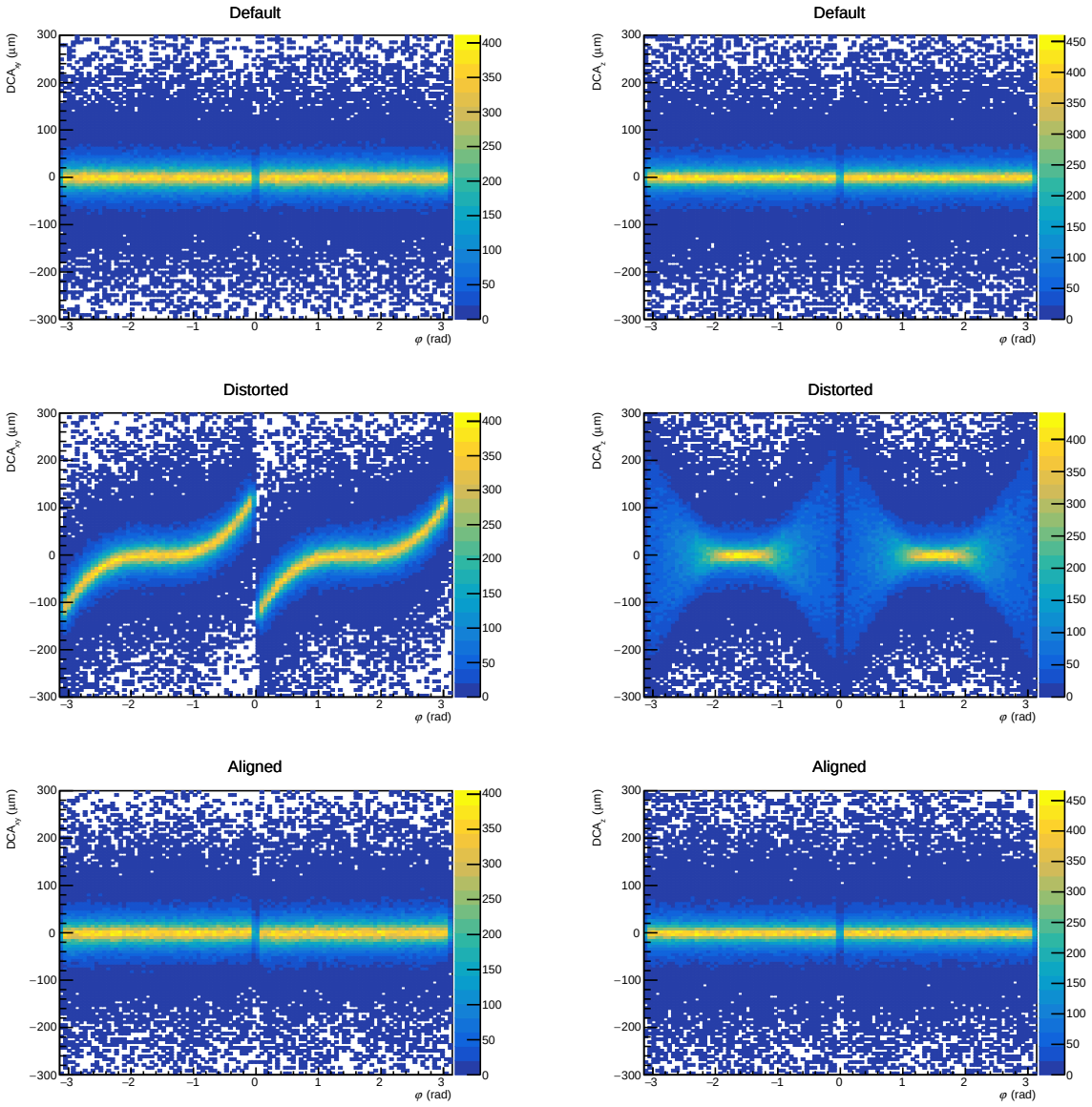

Figure C.1: Panels displaying two-dimensional histograms of the DCA versus the azimuthal angle, φ.

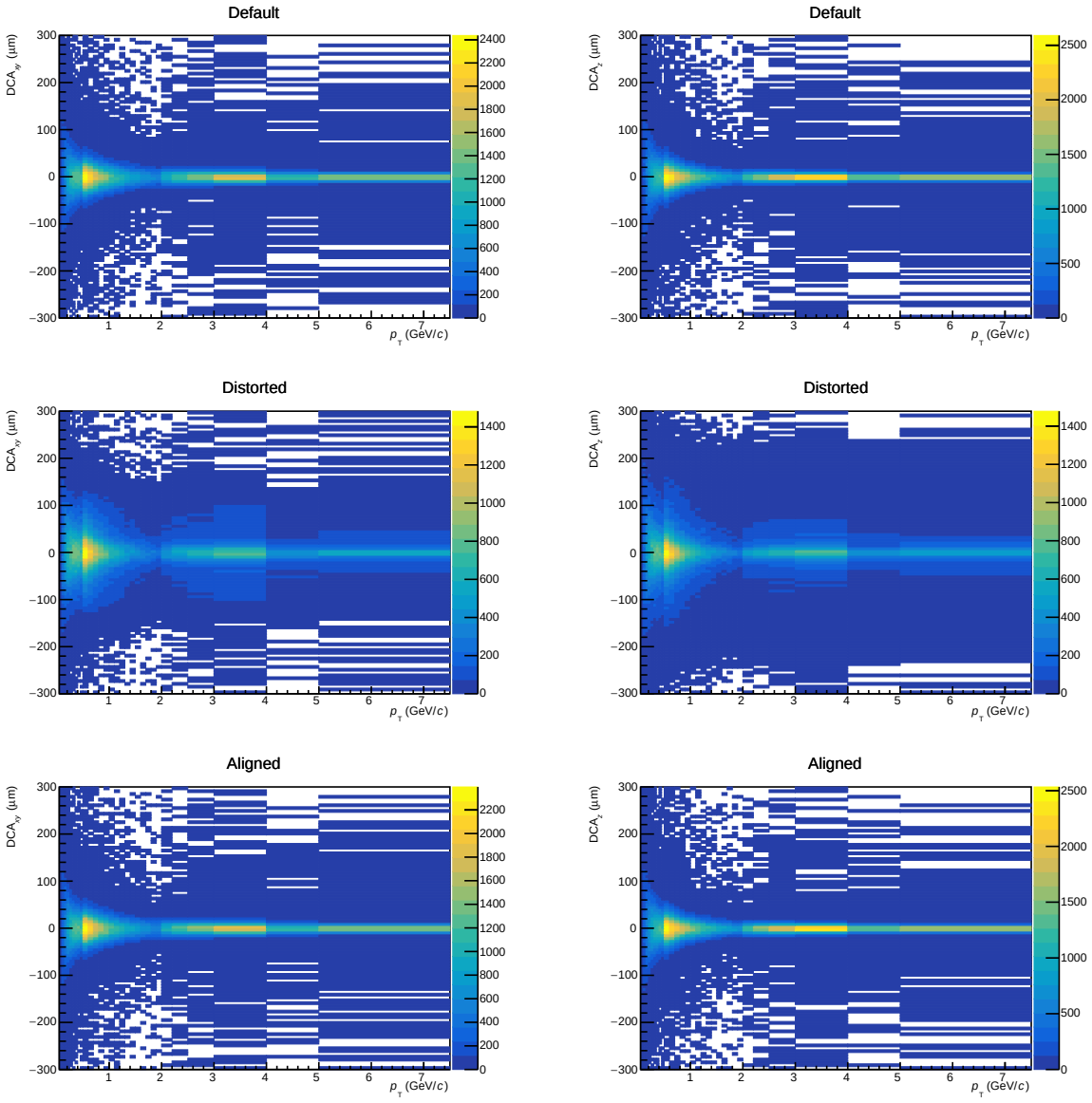

Figure C.2: Panels displaying two-dimensional histograms of the DCA versus the transverse momentum, p_T.

D Two-dimensional histograms of the DCA versus φ for positive and negative tracks separately

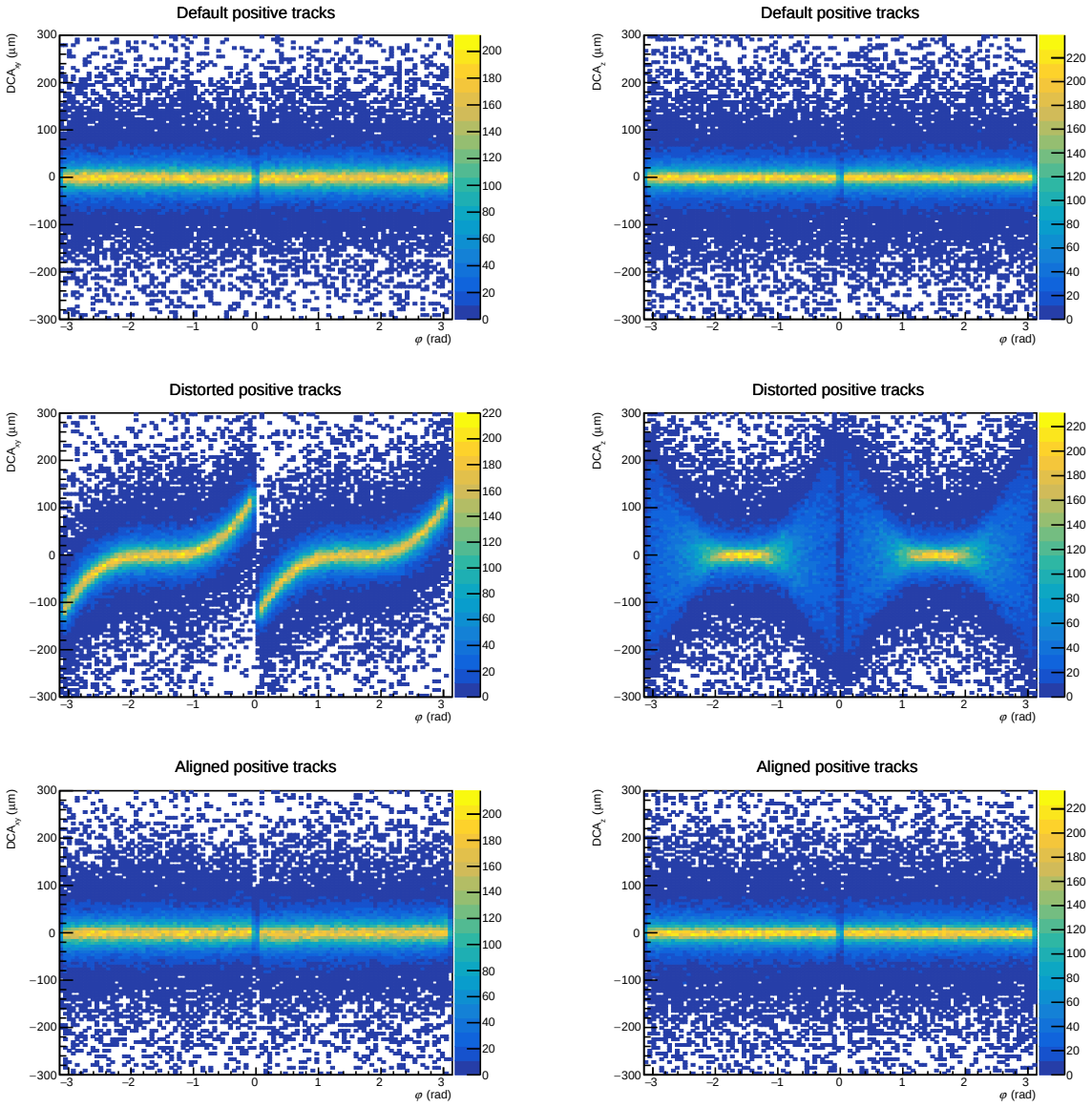

Figure D.1: Panels displaying two-dimensional histograms of the DCA versus the azimuthal angle, φ, for positive tracks.

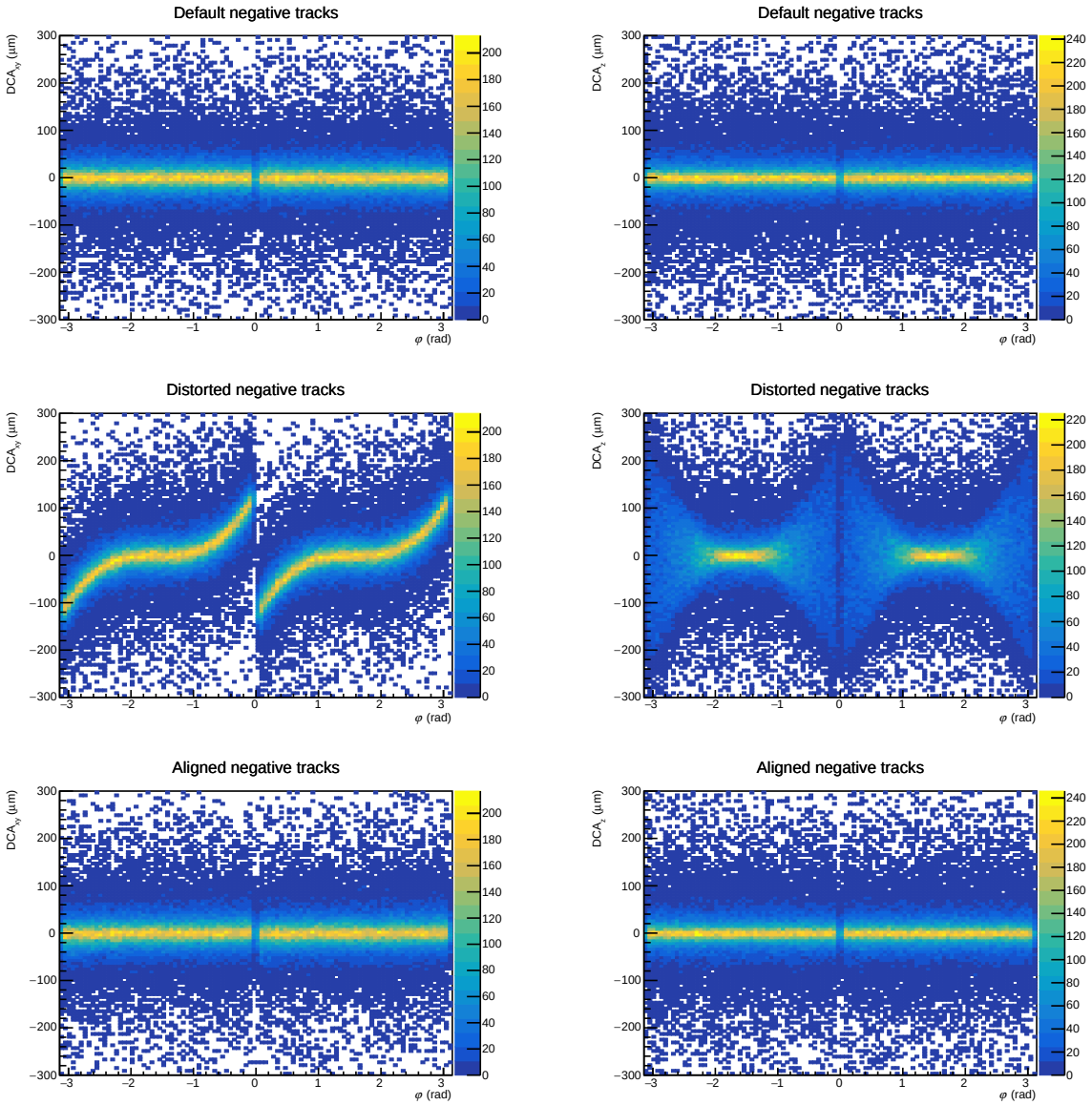

Figure D.2: Panels displaying two-dimensional histograms of the DCA versus the azimuthal angle, φ, for negative tracks.

E Two-dimensional histograms of $\Delta p_T/p_T$ versus generated p_T

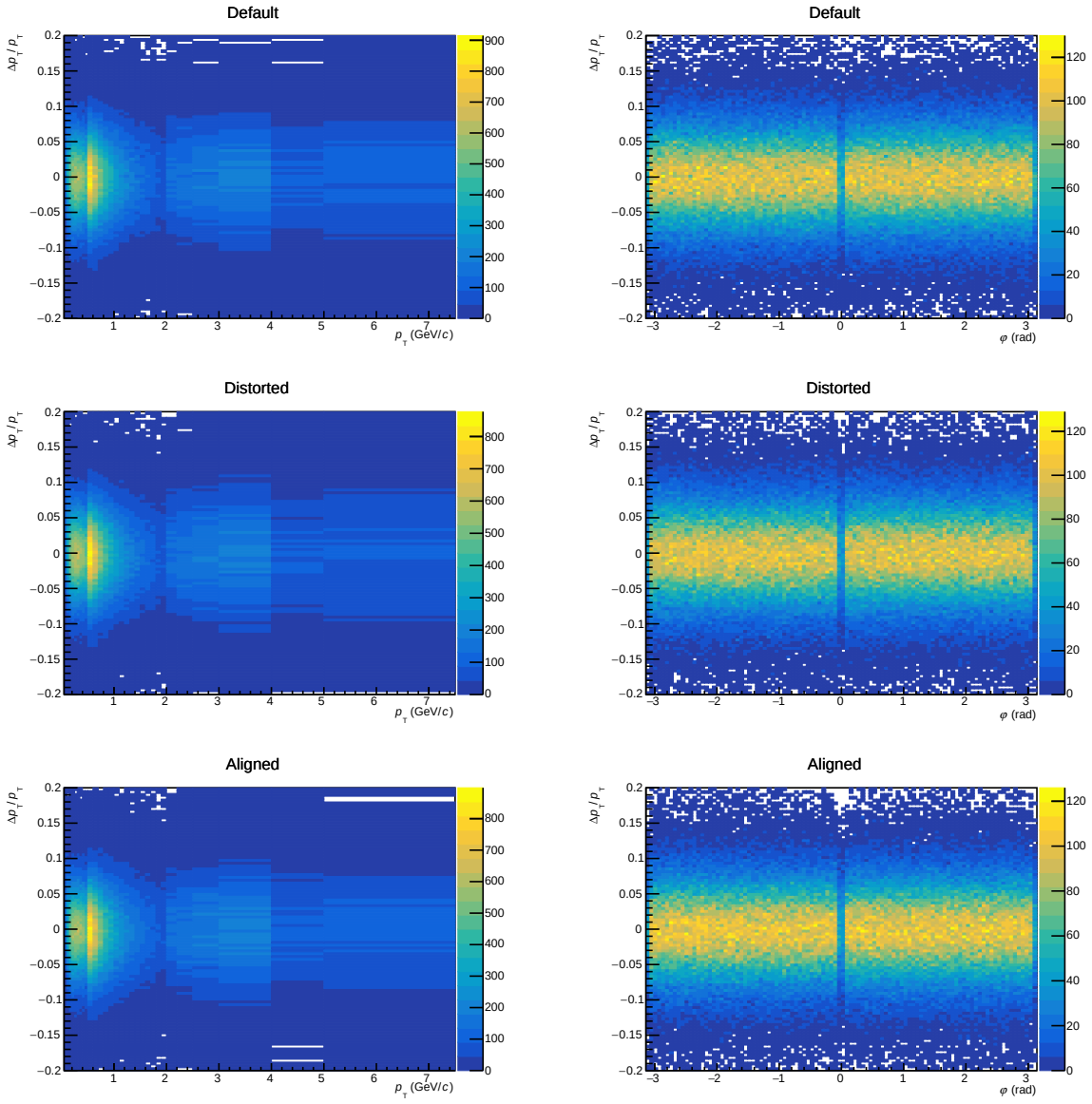

Figure E.1: Panels displaying two-dimensional histograms of the DCA versus the transverse momentum, p_T (left panels), and the azimuthal angle, φ (right panels).